Field effect controlled magnetism and magnetotransport in low dimensions

Liang, Lei

Submitted to *Science Advance*:
Lei Liang, Qihong Chen, Jianming Lu, Wytse Talsma, Juan Shan, Graeme R. Blake, Thomas T. M. Palstra, Jianting Ye– "*Inducing ferromagnetism and Kondo effect in platinum by paramagnetic ionic gating*", 2016 (in review)

Chapter 2

Inducing Ferromagnetism in Platinum by Paramagnetic Ionic Gating

Electrically controllable magnetism, which requires the field-effect manipulation of both charge and spin degrees of freedom, has attracted growing interest since the emergence of spintronics. In this chapter, I will report the reversible electrical switching of ferromagnetic (FM) states in platinum (Pt) thin films by introducing paramagnetic ionic liquids (PILs) as the gating media. Gating using PILs controls the movement of ions in the presence of adjacent magnetic moments, which induces itinerant ferromagnetism in Pt films with large coercivity and perpendicular anisotropy. The field induced FM state in a non-magnetic metal indicates that paramagnetic ionic gating can control electric and magnetic properties simultaneously, which could serve as a versatile tool to induce transport phenomena contributed by mixed degree of freedoms at PIL/solid interfaces.

2.1 Introduction

2.1.1 Electrical control of magnetism

It is often accepted that the properties of magnetic materials are settled after been prepared and are not able to be altered afterward. Although enormous successes have been achieved in information technology, such as the discovery of giant magnetoresistance that boosts the development of data storage devices with large capacity, it is mostly based on magnetization reversal while the magnetic medium itself remains unchanged. On the other hand, the ability of externally controlling the properties of magnetic materials would be highly desirable in view of the next generation spintronic devices. Among all possible approaches, electric field control is the simplest and most straightforward approach.

The ongoing quest to control magnetism by electric field has attracted growing interest in both fundamental sciences and technological applications [1-5]. In diluted magnetic semiconductors, switching magnetization can be achieved by modifying the density and type of carriers with external electric field [5-7]. In multiferroic materials, the electric polarization can couple with the magnetization due to exchange striction effects [8-10]. However, both aforementioned approaches require strong electric field and usually reach magnetic ordering below room temperature making them less feasible for applications. The materials showing high ***Curie* temperatures** (T_C) are generally metallic, which is difficult to manipulate by the field effect due to their intrinsically large carrier densities and consequently short ***Thomas-Fermi* screening lengths**. The application of ionic liquids (ILs) on gating (Fig. 1.1) has achieved inducing quantum phase transitions in many insulator [11-13] and semiconductors [14, 15]. Large amount of carriers accumulated by ionic gating can even tune the metallic devices [16-19]. However, so far ionic gating can only gradually vary the metallic FM materials [2, 3, 17], without realizing dramatic changes such as ON/OFF switching of FM states.

2.1.2 Magnetism at molecule/metal interface

The research field of organic **spintronics** flourishes after the success of fabricating an organic spin-valve [20]. The experiment is based on an organic spacer layer made of π-conjugated organic semiconductor Alq_3, which is sandwiched between two ferromagnetic electrodes Co and $La_{0.67}Sr_{0.33}MnO_3$. The results demonstrate that the injection, transport and detection of spin-polarized carrier, which are main ingredients of spintronics, can be achieved through molecular interfaces.

It has been demonstrated as well that the electronic states of non-magnetic materials, such as diamagnetic copper or paramagnetic manganese, is possible to be altered via charge transfer at the metal/C_{60} interface [21]. **Low-energy muon spin spectroscopy** indicates localized spin-ordered states at the metal-molecule interface.

Density functional theory further suggests the mechanism to be magnetic hardening of the metal atoms due to electron transfer.

There is also report on forming an antiferromagnetic coupling between paramagnetic Fe-porphyrin molecules and ultrathin ferromagnetic Co and Ni magnetic films on a Cu substrate [22]. This study unveils the possibilities of switching metal-ion spin from antiparallel to parallel respective to the substrate magnetization by spin-polarized current.

Perpendicular magnetic anisotropy of Co is of interest for not only fundamental science but also technological applications. Besides the common method of fabricating Pt/Co bilayer causing interface hybridization of normal metal layer $5d$ orbital with Co $3d$ orbitals, organic molecules with π-bond (Pentacene, Alq_3, C_{60}) can also react with $3d$ electrons of Co [23]. The study suggests that this process is governed by the nature of the chemical bonds between the organic molecules and the magnetic electrodes at the interface.

Tunneling magnetoresistance effect has been observed in devices based on molecules, such as zinc methyl phenalenyl that has no net spin. The asymmetric magnetoresistance arises from the independent magnetization switching of the magnetic molecular dimer with respect to the hybridized surface Co layer [24].

To sum up, the formation of chemical bonding at the molecule/metal interface via orbital hybridization between d electrons in metal and molecular π-bonded p electrons serves as an alternative and effective approach to change the electronic and magnetic state of metals once they have been made.

2.2 Concept

2.2.1 Two-dimensional ferromagnetism

Magnetism at low dimensionality has been studied extensively and continues to be a subject for its importance in both fundamental and technological interest. Theoretically, a two-dimensional magnet with isotropic short-range interaction does not exist according to the ***Mermin-Wagner-Berezinskii*** theorem, which demonstrates that in dimensions $d \leq 2$, thermal fluctuations prohibit the long range magnetic ordering at finite temperature in an isotropic system. However, there are a few exceptions of (quasi-) two-dimensional magnets discovered, due to particular parameters.

2.2.2 Stoner criterion of band ferromagnetism

Ferromagnetism ultimately stems from the **Coulomb interaction**. Physically, the Stoner model of band ferromagnets explains spontaneous spin splitting in FM metals such as Fe, Co and Ni, and can be formulated in terms of dispersion relations for spin up and down electrons:

$$E_{\uparrow}(k) = \varepsilon(k) - I\frac{N_{\uparrow} - N_{\downarrow}}{N}, \tag{2.1}$$

$$E_{\downarrow}(k) = \varepsilon(k) + I\frac{N_{\uparrow} - N_{\downarrow}}{N}. \tag{2.2}$$

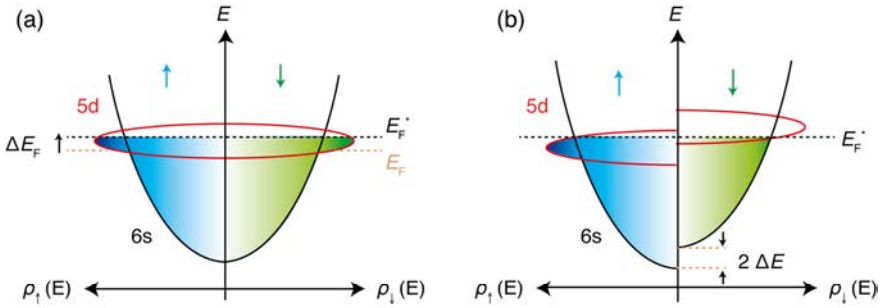

Figure 2.1 (a) The dispersion relation of a 5*d* metal showing density of state close to Fermi level. The dash lines denote the Fermi level prior to (brown) and after (black) gating. **(b)** Density of states showing spontaneous splitting of energy bands without an applied magnetic field. The blue and green colors illuminate the up (↑) and down (↓) spin electrons.

2

Here, the second term accounts for the exchange energy, where I is the exchange integral, $N_\uparrow$ and $N_\downarrow$ the number of up and down spin electrons, which are given by $N_\uparrow = \frac{1}{2}(N - \rho_F \Delta E_F)$ and $N_\downarrow = \frac{1}{2}(N + \rho_F \Delta E_F)$, where N, ρ_F and ΔE_F represent the total number of electron, the density of states at Fermi level and the change of the Fermi energy by electric field, respectively. The situation is illustrated in Figure 2.1.

When gating lifts the Fermi energy from E_F to E_F^*, the kinetic energy gained is

$$\delta E_k = \frac{1}{2}\rho_F (\Delta E_F)^2. \tag{2.3}$$

However, this process also costs potential energy due to the interaction of the magnetization with the molecular field, given by

$$\delta E_p = -\int_0^M \mu_0(\lambda M) dM = -\frac{1}{2}\mu_0 \lambda M^2, \tag{2.4}$$

in which $M = \mu_B(N_\uparrow - N_\downarrow)$, μ_0 and λ are the permittivity and molecular field, respectively. The exchange integral I is a measure of the Coulomb energy, linked to λ by $I = \mu_0 {\mu_B}^2 \lambda$.

Hence, the total energy change will be

$$\delta E = \delta E_k + \delta E_p = \frac{1}{2}\rho_F (\Delta E_F)^2 (1 - I\rho_F). \tag{2.5}$$

For spontaneous spin polarization to occur, $\delta E < 0$, which requires the product of ρ_F and I larger than unity:

$$I\rho_F > 1 \ . \tag{2.6}$$

This is called the **Stoner criterion**.

2.2.3 Hall effect family and anomalous Hall effect

Anomalous Hall effect (AHE) is a member of the Hall effect family. Let us briefly review the history of the discovery of the Hall family members. *Edwin H. Hall*

discovered the ordinary Hall effect in 1879 [25], which he stated when a current-carrying conductor was placed in a magnetic field, the Lorentz force "pressed" its electrons against one side of the conductor. Two years later, he reported that this effect was ten times larger in ferromagnetic iron [26], which was the main character of this thesis: the AHE. Since then, the Hall effect becomes a simple elegant tool to measure carrier type, density and mobility of materials and the AHE is widely used to demonstrate the existence of ferromagnetism. So far, the Hall effects mentioned above require two types of external conditions, which are magnetic field B and magnetization M. Can electric current flow perpendicularly to the electric potential gradient without any external forces? The answer is yes when strong spin orbit interaction is presence.

Spin Hall effect (SHE) refers to such an effect that the spin-up and spin-down carriers accumulate at the opposite edges of the sample without external B field. It was first predicted by *Dyakonov* in 1971 [27] and was experimentally proved until 2004 [28]. SHE can be regarded as two copies of AHE for carriers with different spin, where both effects are related with the **spin-orbit interaction**.

Another branch of the Hall family is the quantized version of the Hall effect. In 1980, the integer **quantum Hall effect** (QHE) was first observed by von Klitzing with strong external magnetic field [29]. The well-defined Hall plateaus manifest the formation of Landau levels caused by B field. When the Fermi level of the systems lies between two neighboring Landau levels, the bulk carriers are localized, while the electron can propagate along the edge of the sample, which is dissipationless and might be useful for fabricating low energy consumption devices.

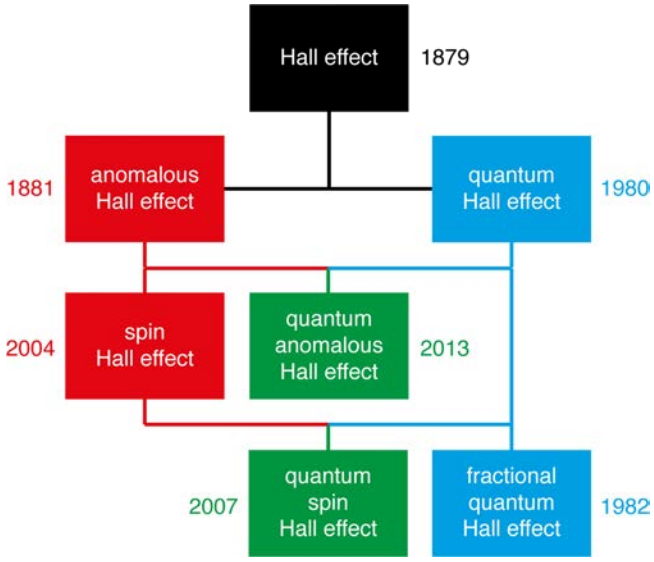

Figure 2.2 The family tree of the current known Hall effect and the corresponding discovering time.

Two years later, when the device of two-dimensional electron gas with even higher mobility and at lower temperature down to 0.5 K, the fractional plateaus were found by *Daniel Tsui* and *Horst Störmer* [30]. This was interpreted by *Robert Laughlin* as a new quasiparticle state formed by electrons binding magnetic flux [31].

When the quantized version of Hall effect gets married with its relatives with strong spin-orbit interaction, new offsprings will be generated. The first breakthrough was the discovery of **quantum spin Hall effect** by *Zhang* [32] and *Molenkamp* in 2007 [33], although the concept had been proposed by *Kane* in 2005 [34] in graphene.

The coming of the last one of the quantized Hall effect trio, the **quantum anomalous Hall effect**, was a bit late. Previous work focused on the pioneering Haldane model of graphene in a periodic magnetic field with zero net magnetic flux. However, this is too weak to be observed in practical system. In 2013, the emergence of topological insulator opened a new avenue to realize it and eventually it was observed by *Que*, *et al* [35].

Among all of the aforementioned members of Hall effect, the understanding of the AHE takes the longest period of time. The reason behind is that the AHE problem involves concepts based on topology and geometry that have been recently formulated. Another reason is that experimentally, the variety of AHE systems is rich and complex.

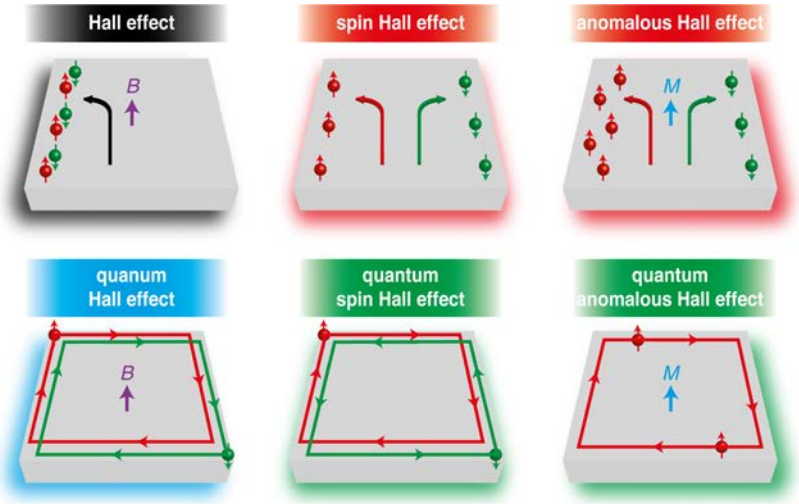

Figure 2.3 Members of the Hall family. Red and green balls with small arrows denote the electrons with up and down spins. The blue and purple arrows show the direction of the magnetization and external magnetic field directions. The big arrows represent the electron current direction of up and down spins.

Reviewing the history of the theoretical studies of AHE, three main mechanisms have been proposed. The first one is the intrinsic mechanism. Initially proposed by *Karplus* and *Luttinger* (KL) as the electrons acquire an additional *anomalous velocity* perpendicular to the electric field [36] and recently formulated by *Chang* and *Niu* as the **Berry curvature** [37].

The KL theory centered on the perfect crystal, whereas another two mechanisms focused on the influence of disorder scattering. In 1955, *Smit* proposed a theory that ascribed origin of the AHE to the asymmetric scattering from impurities due to spin-orbit interaction [38]. *Berger*, on the other hand, argued that the electrons experienced opposite electric fields approaching and leaving an impurity [39]. The AHE has become an attractive topic ever since and been reported in numerous systems despite that its physics remains an enigmatic problem until now.

Empirically, the AHE can be described by

$$\rho_{xy} = \rho_{xy}^{0} + \rho_{xy}^{A} = R_0 B + R_A \mu_0 M \,, \tag{2.7}$$

where B is the magnetic field, M the magnetization and R_0, R_A the ordinary and anomalous **Hall coefficients**, respectively. The first term denotes the ordinary Hall effect and the second term represents the AHE. We will utilize this equation frequently in the following sections and chapters.

2.3 Experiment

2.3.1 Device fabrication and transport measurement

Transistor devices used for PIL gating were all fabricated by standard micro-fabrication. Using **electron beam lithography** (EBL), we defined a Hall bar of 3×7 μm^2. All metal channels (Pt, Pd, and Au) were prepared by DC **magnetron sputtering** (Kurt J. Lesker) after pumping the chamber below 1.0×10^{-8} mbar. Sputtering powers (50 to 200 W) and duration (2 to 12 s) were optimized for preparing films of different thicknesses.

Separately, contact electrodes comprising bilayer Ti/Au (5/70 nm) were deposited onto the patterned Hall bars using e-beam evaporation (Temescal FC-2000) below 1.0×10^{-6} mbar. Afterwards, an Al_2O_3 isolation layer (30 nm) was deposited to cover all contact electrodes, limiting the gating effect only to the exposed channel surface.

Low temperature electrical transports were measured in a helium cryostat (PPMS, Quantum Design) under out-of-plane magnetic fields up to 6 T. All transport properties were measured by two lock-in amplifiers (SR830, Stanford Research) using a constant AC current excitation of 50 μA at 13.367 Hz. The voltage bias on BMIM[$FeCl_4$] (the PIL used in all gating experiments) was applied by a source measure unit (Model 2450, Keithley).

2.3.2 Paramagnetic ionic liquid

We have introduced the ionic gating technique in chapter 1. Despite the fact that ionic gating is capable of tuning large amount of carriers, it is highly demanding to realize the field-effect control of the spin degree of freedom.

In this chapter, paramagnetic ionic liquids (PILs), composed of anions containing transition metal with unpaired *d*-orbitals, are introduced as gating media to induce magnetic interactions at the gated channel surface (Fig. 2.4). Therefore, it extends the conventional ionic gating to the spin tunability: the second intrinsic characteristic of the electron.

Replacing the organic anions with metal complexes maintains the general physicochemical properties of ILs, such as low melting temperature ($T_m < 200$ K), negligible vapor pressure, and large electrochemical window, which are prerequisites for ionic gating. Guided by these crucial requirements, butylmethylimidazolium tetrachloroferrate (BMIM[$FeCl_4$]) was synthesized for all experiments discussed afterwards (Fig. 2.5).

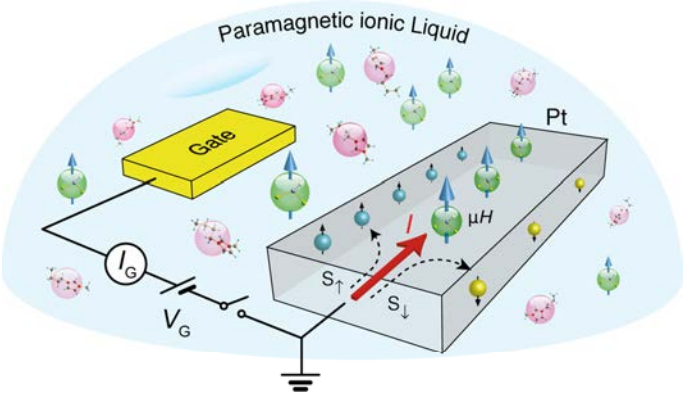

Figure 2.4 Schematic diagram of ionic gating with PIL and transport measurement setup.

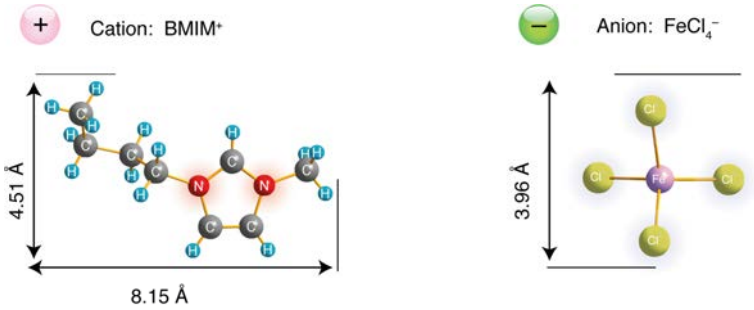

Figure 2.5 Composition of PILs: $BMIM^+$ (cation) and $FeCl_4^-$ (anion). The dimensions here were determined from single crystal X-ray diffraction data at 100 K.

2.3.3 Magnetic property

In BMIM[$FeCl_4$], all five $3d$ orbitals of Fe^{3+} in the anions are unpaired giving a total spin quantum number of $S = 5/2$ (high spin state). The temperature dependence of magnetization of BMIM[$FeCl_4$] between 2 to 350 K was measured in a **SQUID** magnetometer (MPMS XL-7, Quantum Design) up to 7 T. The curves show no hysteresis loop and follow the Langevin equation, indicating paramagnetic nature (Fig. 2.6a). This PIL with considerable large moment (~5.9 μ_B/Fe^{3+}) responds actively to external magnetic field even at room temperature (Fig. 1.9b).

The temperature dependent magnetic susceptibility (χ-T) measurement was performed after zero-field cooling down to 2 K and the data were taken at $B = 0.1$ T during warming up. BMIM[$FeCl_4$] shows paramagnetic with large effective moment $\mu_{eff} = 5.87\ \mu_B$ following **Curie's law** down to 2 K (Fig. 2.6b).

Below 100 K, signatures of weak antiferromagnetic interactions were observed (Fig. 2.6c) [40]. However, no long range magnetic ordering was established down to 2 K, the lowest temperature accessed in our measurements.

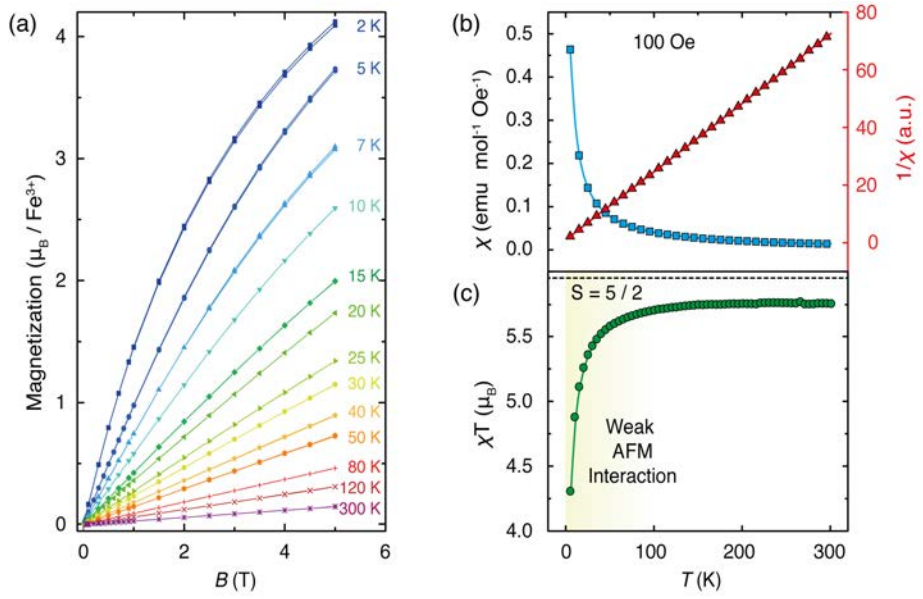

Figure 2.6 (a) Temperature dependence of the magnetization curves for BMIM[$FeCl_4$]. **(b)** Temperature dependence of the magnetic susceptibility χ. **(c)** Temperature dependence of the product (χT) of magnetic susceptibility and temperature.

2.3.4 Paramagnetic ionic gating and temperature dependence resistance

Figure 2.7 shows the **transfer curve** of the PIL-gated Pt. The gate voltage V_G dependence of the sheet resistance R_s (device A, thickness t = 8 nm) shows that the R_s can be reversibly controlled by sweeping V_G with negligible leak current I_G (Fig. 2.7 bottom panel). The reversible gating response of the sheet resistance R_s is consistent with the linear leak current I_G indicating no signature of redox reaction. The electrostatic nature of gating was further confirmed by chronoamperometry experiment (Fig. 1.6) and subsequent control experiments in the supplementary information of this chapter.

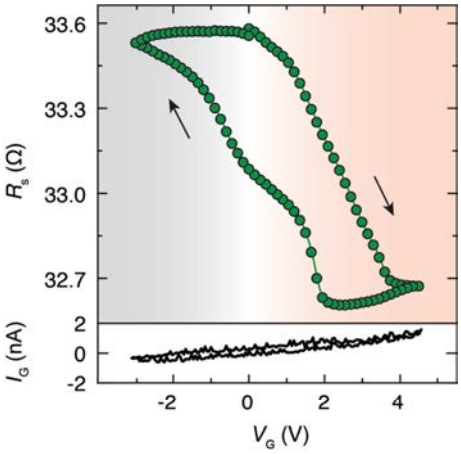

Figure 2.7 Typical transfer curve of Pt film (device A, t = 8 nm) with a full gating cycle from -3 to 4 V at a sweeping rate of 50 mV s^{-1}.

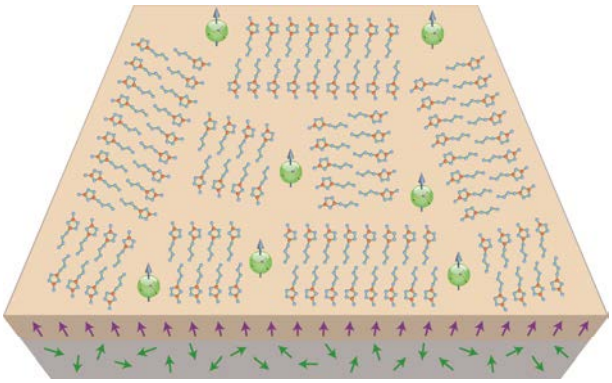

Figure 2.8 Cations are driven towards the surface of Pt forming ordered domain patterns after applying positive V_G, which leaves the domain interstitials filled with anions [41]. The purple and green arrows denote the spin configuration of the surface and bulk Pt after PIL gating.

After applying positive V_G until R_s saturates, cations are driven towards the surface of Pt and form patterns leaving interstitials filled with anions [41] (Fig. 2.8). This surface morphology has a close relation with the formation of magnetic domains in the later sections.

Figure 2.9 shows the five consecutive procedures as a correlation between emergence of ferromagnetism and R_s as a function of temperature. We first applied V_G = 4V at 220 K, which is slightly above the frozen temperature of PIL enabling the ionic mobility of ions as well as minimizing the kinetic of side reactions. After observing a prominent R_s drop, device A was cooled down to 2 K at 2 K min^{-1} followed by the Hall resistance R_{xy} measurement (showing FM ON state in Fig. 2.9a).

After retracting V_G, device A was warmed up to 260 K and R_s coincided with that measured on cooling down until 200 K. With further increasing temperature, the PIL started to melt and R_s gradually increased as the gating effect diminishes with redistribution of the ions. At 220 K, R_s (in red) had exactly the same value as that before gating (in black); this indicates that the whole gating process is non-faradaic. Finally, after fully relaxation of the PIL at 260 K, the device was cooled down back to 2 K without V_G and the Hall resistance R_{xy} was measured (indicating as FM OFF state in Fig. 2.9a).

The emergence of the ferromagnetism is demonstrated by the appearance of **hysteresis loop** in the AHE at 2 K and will be further discussed in the following sections.

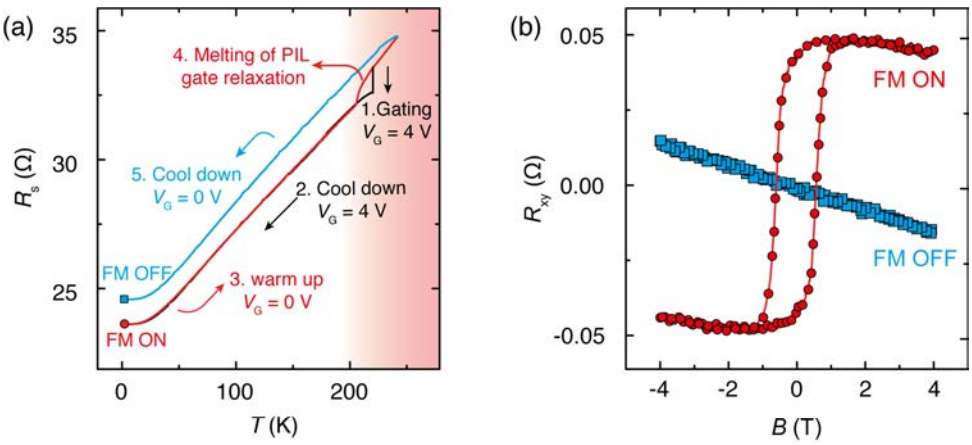

Figure 2.9 (a) Correlation between ferromagnetism and R_s as a function of temperature for five consecutive procedures. **(b)** Hall resistance R_{xy} at 2 K with/without applying V_G by the procedures described in (a). The FM ON and FM OFF denote R_{xy} with a hysteresis loop for the FM state and a linear dependence for the PM state.

2.4 Results and Discussion

2.4.1 Band structure of the ionic gated Pt

Platinum (Pt) is normally regarded as an exchange-enhanced paramagnetic (PM) metal on the verge of FM instability. Hence, applying electric field could induce the FM state in Pt if the enhanced product $I\rho_F$ satisfies the **Stoner criterion**, which might subsequently evokes dramatic changes in both magnetism and electrical transport. Meanwhile, decreasing the coordination number of nearest neighboring atoms at the surface results in reduced electronic bandwidth. Consequently, ferromagnetism can be induced when the product of I and ρ_F is strongly enhanced by reducing dimensionality [42]. For example, although not electrically controllable, the isolated Pt nanoparticles show ferromagnetism if their surfaces are perturbed by chemisorption [43].

According to *ab initio* calculation, the DOS peak of Pt lies slightly below the **Fermi level** (E_F) [44]. Therefore, it is expected that depleting carriers with negative V_G by driving the magnetic anions towards the Pt surface might satisfy the Stoner criterion by increase both ρ_F and I because of the possible d–d interaction between Pt and $FeCl_4^-$. However, the negatively gated Pt maintains the PM state despite the increase of $|R_{xy}/B|$ (Fig. S2.1). In contrast, FM states can be induced when the transfer curve shows an obvious drop at $V_G > 0$ (Fig. 2.7), evidenced by the anomalous Hall effect (AHE) with clear hysteresis (Fig. 2.9b). This finding is consistent with other reports of the electric-field tuning of magnetic moments in systems with Stoner enhancement, where a positive V_G increases magnetic parameters such as **saturation magnetization** (M_s), **coercivity** (H_c) and **Curie temperature** (T_C) [3, 19].

As reported in many other material systems [11, 12], ionic gating can cause significant change of carrier density due to its strong field effect. Here, the apparent carrier density measured by the Hall effect n_{Hall} (e.g. extrapolated from R_{xy}/B) at 5 K significantly increases from 1.68 to 3.24×10^{17} cm^{-2} upon applying $V_G = 4$ V. Since the actual change of carrier density is caused by the formation of electric double layer, the upper bound of the doping concentration can be simply determined by counting the number of ions accumulated at the channel surface. Direct imaging of ion-gated **gold** (Au) surface by **scanning tunneling microscopy** [41] shows that the maximum induced carrier density is limited to $\sim 5 \times 10^{14}$ cm^{-2} (Fig. 2.8). Therefore, the large discrepancy between the carrier density estimated from the surface ion concentration and Hall effect indicates that n_{Hall} may not be a suitable indicator to quantify the actual change of carriers.

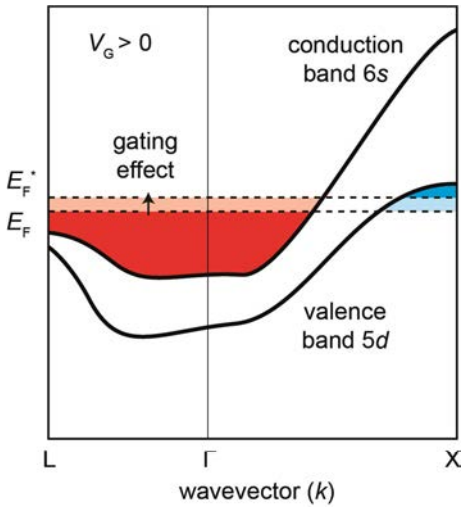

Figure 2.10 Field-effect tuning of E_F in the simplified band structure of Pt, where the Fermi surface of pristine Pt is composed of 5*d*-states at X points and the 6*s*-state near the Γ point in the Brillouin zone. Applying a positive V_G lifts the Fermi level (to E_F^*) and fills the 5*d*-band, which changes the conductivity ratio σ_h/σ_e significantly.

Despite the quantitative difference, large Δn_{Hall} implies substantial change of E_F, which is comprised by the 6*s* electron-like and 5*d* hole-like pockets in open and nearly closed Fermi surfaces, respectively [45-47] (Fig. 2.10). Positive V_G lifts E_F accompanying with the increase of 6*s* electrons (n_e) and decrease of 5*d* holes (n_h). Because of their opposite Hall coefficients, changes of n_e and n_h contribute destructively to the transverse resistance R_{xy} [48] causing seemingly large Δn_{Hall}. Because of the elevated E_F at $V_G > 0$, the conductivity enhances by having more 6*s* electrons with higher mobility. More importantly, the increase of E_F also reduces the available empty 5*d* states, causing less *s*-*d* scattering [49].

Considering the intrinsically large carrier density in Pt and comparably small change of carriers caused by the field effect, observing large ΔR_s reflects the influence mainly by the reduced ratio of n_h/n_e. The FM state can be switch ON and OFF by following different sequences of PIL gating as shown in Figure 2.9. The coincidence between the appearance of AHE (Fig. 2.9) and decrease of R_s (Fig. 2.8) indicates a close relationship between the emergence of ferromagnetism and PIL gating.

2.4.2 Perpendicular magnetic anisotropy

Devices that show a **perpendicular magnetic anisotropy** (PMA) hold promising application in data storage. In metallic thin films, many recipes have been developed. For example, the cobalt film with in-plane easy axis can be converted to PMA when is contacted to platinum [50, 51] or is capped by molecules [23]. Other

examples include strain-induced PMA in $Tm_3Fe_5O_{12}$/Pt bilayer [52] and new materials Mn_3Ge [53], CoCrPt [54], *etc.*

Regarding the determination of magnetic anisotropy of ion-gated Pt thin film, *i.e.* determining the easy-axis of the magnetization, traditionally, the measurement is based on the magnetization curve from magnetometry (such as SQUID). Sample was measured two times with the basal plane parallel and perpendicular to the magnetic field. Along its hard axis, magnetization of the sample is saturated slowly (Fig. 2.11a); whereas is rapidly along its easy axis (Fig. 2.11b).

However, this type of measurement is limited by the device configuration for PIL-gated systems. In order to measure the perpendicular anisotropy electrically from AHE, a pair of top and bottom electrodes should be attached to measure the Hall effect from in-plane B field (Fig. 2.11c). However, in this case, the top electrode will block the direct contact between PIL and Pt channel. Therefore, no field effect could be applied to the covered surface.

Nevertheless, the square shape of the hysteresis loop with the device geometry shown in Figure 2.11d indicates strong PMA (Fig. 2.9b). Because of the strong **screening** in Pt, the field-induced modulation is confined beneath the surface within a-few-Å depth. Together with the aforementioned PMA, the induce FM state mimics the ideal two-dimensional (2D) itinerant **Ising ferromagnetism**.

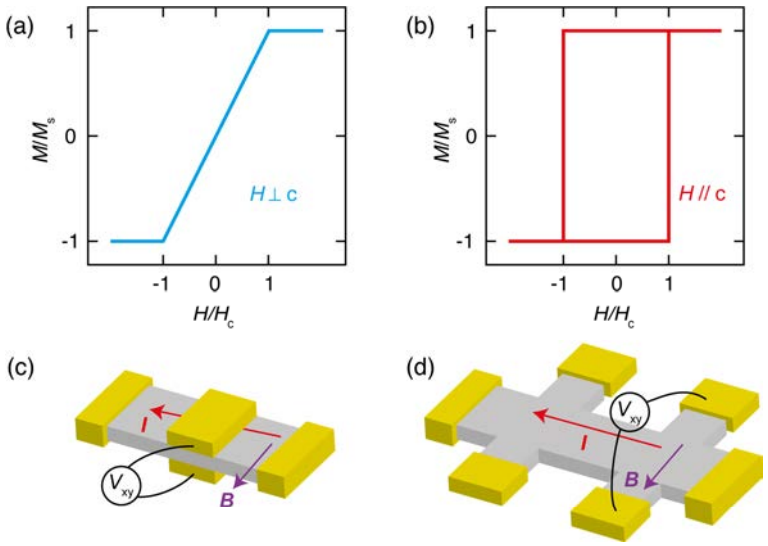

Figure 2.11 The corresponding hysteresis loops in the Stoner-Wohlfarth model for hard axis $H \perp c$ **(a)** and easy axis $H \parallel c$ **(b)**. Device measurement geometry under in-plane B field **(c)** and out-of-plane B field **(d)**.

Magnetic films with PMA are highly pursued in spintronics acting as the exchange bias layers in giant magnetoresistance devices [55], magnetic tunnel junctions [56] and logic devices [57], *etc*. The gate accessible PMA in PIL-gated Pt is technically favorable because of its electrical tunability.

2.4.3 Temperature-dependent anomalous Hall effect

The temperature dependences of the AHE for PIL-gated Pt films with two thicknesses of t = 8.0 nm (device A) and 2.7 nm (device B) are shown in Figure 2.12. The occurrence of ferromagnetism is manifested as AHE with clear **hysteresis loops**.

Empirically, the Hall resistivity in ferromagnets ρ_{xy} can be described by two terms: the ordinary Hall effect ρ_{xy}^{0} and the anomalous part ρ_{xy}^{A}. For the thinner device B, we observed that ρ_{xy}^{A} is one order of magnitude larger than that in device A, indicating a stronger M_s in thinner films. On the other hand, the hysteresis loop of device B is smaller than thicker device A.

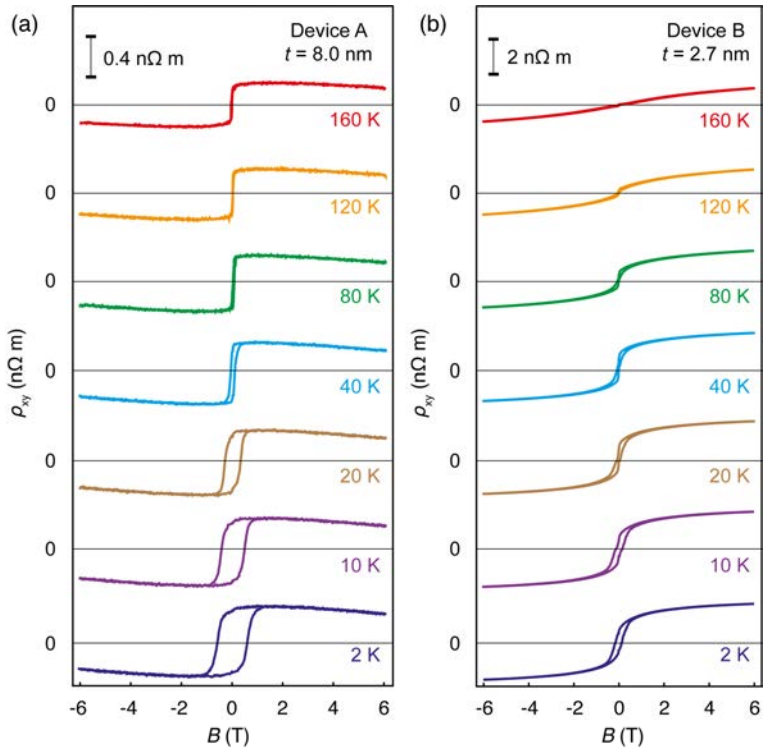

Figure 2.12 Temperature-dependent Hall resistivity ρ_{xy} in FM Pt after PIL gating. Both device A with t = 8.0 nm **(a)** and device B with t = 2.7 nm **(b)** show a deceasing ρ_{xy} and H_C with increasing temperature, while are different in the amplitude of ρ_{xy} and the slope of the linear part of ρ_{xy}.

The coercive force disappears rapidly for both samples while the **saturation magnetization** maintains up to quite high temperature (>160 K). In addition, the magnetization direction is the same for both samples while the slope of the linear part of the Hall effect is opposite for each sample. The sign of the ordinary Hall coefficient indicates the difference of the Fermi surface topology, which remains to be understood with further experimental and theoretical studies.

2.4.4 Gate-dependent anomalous Hall effect

It is worth noting that the strength of the induced FM states are closely linked to the V_G (Fig. 2.13). As shown in Figure 2.13b, the AHE measured for the same device at 5 K shows gradual decrease of the ρ_{xy}^{A} and H_c after being cooled down with different V_G biases reduced from V_G = 4 V, which is consistent with the increase of ordinary **Hall coefficient** R_0 demonstrated in 3.4.1.

The electrostatic nature of the gating is further validated by measuring the AHE at 5 K for the same device cooled down with different V_G (Fig. 2.13a). The change of R_s with respect to V_G is defined as

$$\Delta R_s = R_s(V_G) - R_s(0)\,, \tag{2.8}$$

where $R_s(V_G)$ and $R_s(0)$ are the R_s at finite and zero V_G, respectively. Figure 2.13a shows a typical V_G dependence of R_s at 220 K with a full bias sweep from -3 to 4 V. Clear resistance drop appears under positive gating, which is consistent with other reports [58, 59].

We performed the Hall measurement at different V_G in a typical film (t = 16.0 nm) under out-of-plane magnetic field at 5 K. For achieving each electronic state, the device was first gated to 4 V at 220 K when the R_s approaching saturation. Afterwards, we gradually decreased V_G to the desired values by monitoring the change of R_s. The low ionic mobility at 220 K leads to a hysteretic V_G dependent R_s (Fig. 2.13a). Therefore by decreasing V_G, we can realize better control to reach the desired electronic state by minimizing the change of R_s before actually frozen of PIL.

To measure the Hall effect at five different V_G as shown in Figure 2.13b, we first gated sample to V_G = 4.0 V, which induced the hysteresis loop in AHE at 5 K indicating the existence of ferromagnetism. The sample was then warmed up to 260 K with V_G = 0 V and cooled down to 220 K for repeating identical gating process. With the decrease of V_G, the hysteresis loop in ρ_{xy} (at 5 K) gradual diminished and evolved into a linear dependence of B, indicating the switching off of the FM state. This order of measurement sequences excludes the possibility of forming impurities by the previous gating. Following the continuous tuning of the FM states, the slope of the linear part of the Hall signal observed at high B field increase with the decrease of V_G suggesting a continuous tuning of carriers. On the other hand, the gradual evolution and repeatable access of FM state strongly suggest that the FM state depends on the applied V_G, which is free from magnetic impurities accumulated or reversible, formed by all prior gating procedures.

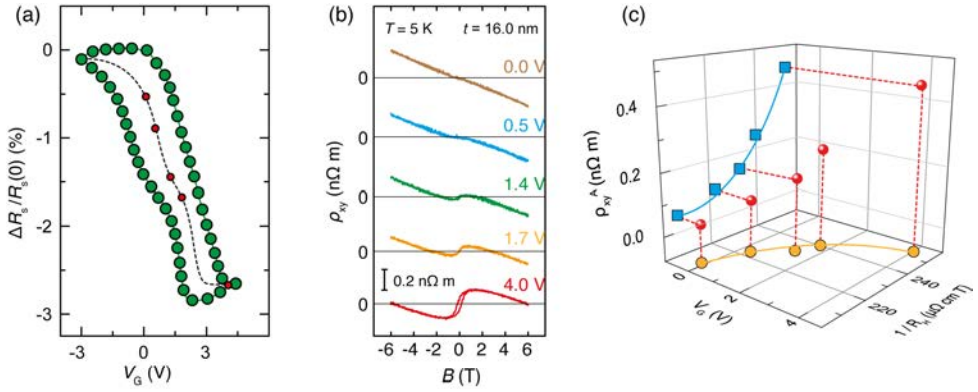

Figure. 2.13 Gate-dependent Hall resistivity ρ_{xy} in FM Pt after PIL gating. **(a)** The transfer curve with red dots showing the gated states that have been cooled down. **(b)** The corresponding AHE effect measured at 5 K for each gated states. **(c)** The correlation between the V_G, ρ_{xy}^A that represents the saturation magnetization and the slope of ordinary Hall effect $1/R_H$ that stands for the change of the carrier number.

2.4.5 Thickness-dependent anomalous Hall effect

As shown in Figure 2.14, the film thickness dependence of ρ_{xy} indicates that the ρ_{xy}^A increases with the decrease of t. For films with $t > 24.0$ nm, the AHE signal cannot be distinguished from the linear ρ_{xy} because the short screening length isolates the gating effect from affecting the bulk of gated Pt films, which remains PM with linear Hall response. With the increase of t, the enlarging bulk contribution acts as a short circuit channel bypassing the top-most FM layer resulting the reduction of ρ_{xy}^A.

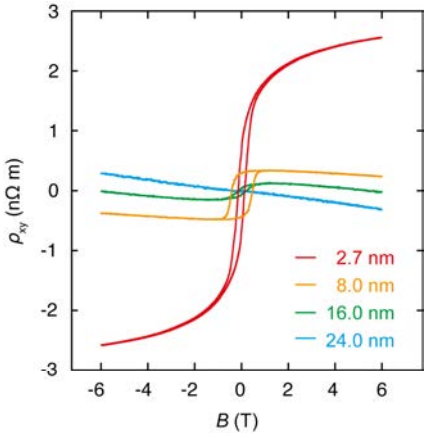

Figure 2.14 The thickness-dependent Hall resistivity ρ_{xy} as a function of B for several Pt films.

Despite the larger ρ_{xy}^{A} in thinner films, the largest H_c was observed for t = 8.0 nm. Since the H_c is closely related to the formation of magnetic domains in different film morphologies, the optimization of the density and rigidity of domain walls at this intermediate thickness might give rise to the largest H_c.

In addition, the ordinary Hall coefficient changes sign at t = 2.7 nm. These observations indicate a modification of the band structure with decreasing thickness, which enhances the Stoner instability in Pt (Pd) films [60].

2.4.6 Strong spin-orbit interaction

Since Pt is a heavy metal, besides the Stoner criterion, we should also take into account the effect of the **spin-orbit interaction** (SOI). The SOI in an atom arises as follows. Consider an electron orbiting a nucleus; from the electron point of view, the orbiting nucleus constitutes a current that gives rise to a magnetic field (from *Biot-Savart* law) equal to

$$\hat{B}_l = \frac{Ze\mu_0}{4\pi r^3 m_0}\hat{L}\,, \tag{2.9}$$

where Z is the atomic number, e the elementary charge, μ_0 the vacuum permeability, m_0 the elementary mass of electron, r the radius of the orbit.

In addition, the magnetic moment by electron spin is given by

$$\hat{\mu}_s = -g\frac{e}{2m_0}\hat{S}\,, \tag{2.10}$$

where g is the Landé g-factor. Therefore, the spin-orbit energy can be represented as

$$\mathcal{H}_{SO} = -\frac{1}{2}\hat{\mu}_s \cdot \hat{B}_l = \frac{gZe^2\mu_0}{8\pi r^3 m_0^2}\hat{L}\cdot\hat{S}\,. \tag{2.11}$$

On the other hand, the total angular momentum operator is given by

$$\hat{J} = \hat{L} + \hat{S}\,. \tag{2.12}$$

Taking the dot product of $\hat{J}$ with itself, we have

$$\hat{J}^2 = (\hat{L}+\hat{S})(\hat{L}+\hat{S}) = \hat{L}^2 + \hat{S}^2 + 2\hat{L}\cdot\hat{S}\,. \tag{2.13}$$

So the total angular momentum can be described in terms of quantum numbers:

$$\hat{L}\cdot\hat{S} = \frac{1}{2}(\hat{J}\cdot\hat{J} - \hat{L}\cdot\hat{L} - \hat{S}\cdot\hat{S}) = \frac{\hbar^2}{2}[j(j+1) - l(l+1) - s(s+1)], \tag{2.14}$$

where s, l, j are the spin, orbital and total angular quantum number, respectively. Taking Eq. 2.14 back to Eq. 2.11, we get

$$\mathcal{H}_{SO} = a\,[j(j+1) - l(l+1) - s(s+1)]\,, \tag{2.15}$$

where the spin-orbit interaction constant a is defined as

$$a = \frac{gZe^2\mu_0\hbar^2}{16\pi r^3 m_0^2}\,, \tag{2.16}$$

Substituting $\langle r^{-3}\rangle = \int \psi_{n,l,m}^{*}\frac{1}{r^3}\psi_{n,l,m}d\tau$ from the expectation value of hydrogen wave function, we derive

$$a \propto \frac{Z^4}{n^3 l(l+1/2)(l+1)}\,, \tag{2.17}$$

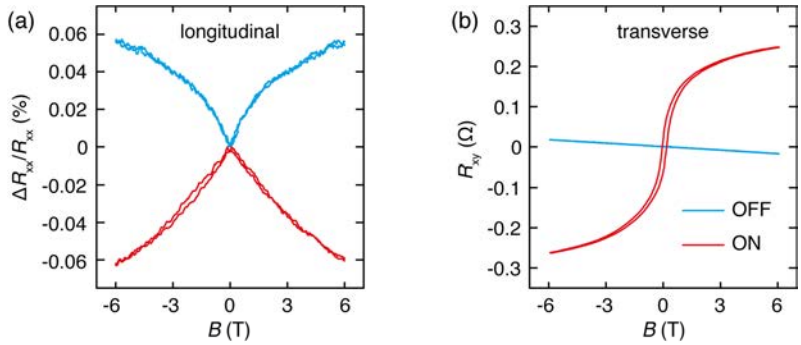

Figure 2.15 (a) Longitudinal magnetoresistance of device B with (red) and without (blue) V_G. **(b)** Corresponding transverse (Hall) resistance of the same device B in PM (OFF) and FM (ON) states at 5 K.

2

which implies that the strength of SOI:

- is proportional to the fourth power of atomic number;
- decreases with increasing quantum number n and l.

Pt is widely used in spintronic devices due to its strong intrinsic SOI and resulting large **spin Hall angle** θ_{SH}. Although AHE was discovered prior to SHE, the former can actually be regarded as two copies of the later, where relativistic spin-orbit coupling generated an asymmetric deflection of the charge carrier depending on their spin direction [61]. The pristine Pt films show **weak anti-localization** (WAL) due to the intrinsically large SOI, resulting in the positive **magnetoresistance** (blue curve in Fig. 2.15a) [62]. When the FM state is switched ON, a negative magnetoresistance appears at low temperature because applying B field in FM state increases the degree of **spin polarization** hence reduces s-d scattering (red curve in Fig. 2.15a). This significant change of the longitudinal transport after gating accompanies with the appearance of the AHE in the transverse measurement (Fig. 2.15b).

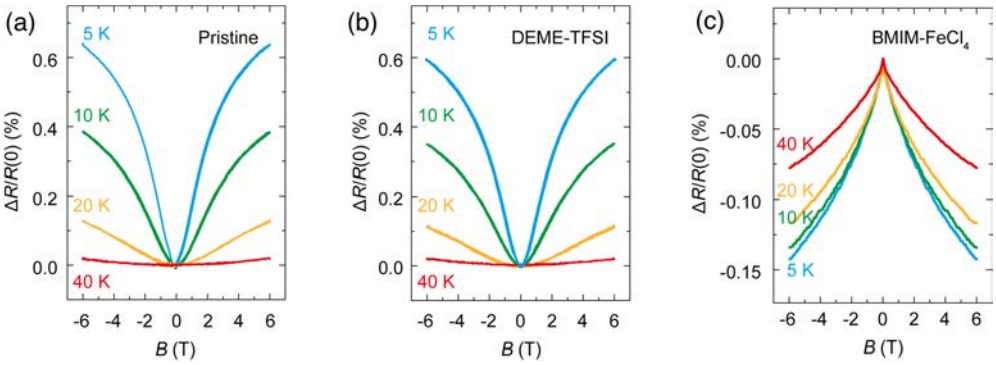

Figure 2.16 Low temperature (T < 40 K) magnetoresistance of **(a)** pristine, **(b)** IL-gated (DEME-TFSI), and **(c)** PIL-gated (BMIM[$FeCl_4$]) Pt films (t = 4.0 nm).

DFT calculation reveals that the Rashba splitting in the heavy metal surface states can be effectively manipulated by shifting the *d*-orbital potential energy by physical implementation [63]. Although compared to the Coulomb field inside the atom, the electric field generated by the electric double layer is weak. However, due to the large SOI of Pt, Rashba effect is another factor to be considered.

To show the different electronic states, we measured the MR below 40 K for pristine, IL-gated, and PIL-gated devices that are all made from a single Pt film (t = 4.0 nm). As shown in Figure 2.16a, the pristine Pt film shows positive MR, which is originated from the WAL due to the strong spin-orbit interaction in Pt. Almost identical MR (Fig. 2.16b) was observed after gating the same Pt film with a typical non-magnetic ionic liquid (N,N-diethyl-N-(2-methoxyethyl)-N-methylammonium bis(trifluoromethylsulphonyl-imide (DEME-TSFI, widely used for ionic gating) in absence of FM state. In contrast, the PIL-gated Pt film shows negative MR in same temperate range (Fig. 2.16c). We ascribe the negative MR to the induced interface ferromagnetism. The intrinsic WAL in Pt and WL caused by interface magnetization causes the WAL to WL crossover as a function of temperature.

2.4.7 Crossover between weak localization and weak anti-localization

Inducing FM states naturally affects other transport properties of Pt, such as the magnetoresistance. The conductivity of conduction electrons σ is determined by the **scattering rate**, given by

$$\sigma = \frac{ne^2\tau}{m^*}, \tag{2.18}$$

where n and m^* are the electron density and effective mass, respectively; τ is the relaxation time of electron and links the electron **mean free path** λ with $\lambda = k_F\tau$ (k_F is the Fermi wave vector), which is influenced by impurity scattering, electron-phonon and electron-electron (Coulomb) interaction.

However, the above semi-classic quasi-particle model ignores the interference of the electron waves. The impurity scattering strength is independent of temperature and screening effect of conduction electron compensates the **Coulomb interaction**. At low temperature, therefore, when the phonon contribution is minimized, interference effect of the electron wave also plays important role and have a **quantum correction** yielding the conductivity

$$\sigma = \sigma_0\left[1 - \frac{1}{\pi k_F l}\ln\left(\frac{\tau_i}{\tau_0}\right)\right] = \sigma_0 - \sigma_{00}\ln\left(\frac{\tau_i}{\tau_0}\right), \tag{2.19}$$

where τ_0 and τ_i are the elastic and inelastic scattering time, respectively; and $\sigma_{00} = e^2 / (\pi h)$.

Applying magnetic field B will induce a magnetic flux Φ_B. When $B > \Phi_B$, those quantum interference will be destroyed, resulting a negative magnetoresistance (hence positive **magnetoconductance**). This is called **weak-localization** (WL) effect. The weak anti-localization (WAL) originates from the

strong SOI, which randomizes the electron spins, resulting in a positive magnetoresistance (hence negative magnetoconductance).

The aforementioned electron localization behavior can be well reproduced by the **Hikami-Larkin-Nagaoka** (HLN) equation [64]. In the low field regime, the conductance variation is given by

$$\begin{aligned}\Delta G(B) = G(B) - G(0) &= \frac{1}{R_s(B)} - \frac{1}{R_s(0)} \\ &= \frac{e^2}{2\pi^2\hbar}\left[\ln\left(\frac{B_\phi}{B}\right) - \psi\left(\frac{1}{2}+\frac{B_\phi}{B}\right)\right] \\ &+ \frac{e^2}{\pi^2\hbar}\left[\ln\left(\frac{B_{SO}+B_e}{B}\right) - \psi\left(\frac{1}{2}+\frac{B_{SO}+B_e}{B}\right)\right] \\ &- \frac{3e^2}{2\pi^2\hbar}\left[\ln\left(\frac{(4/3)B_{SO}+B_\phi}{B}\right) - \psi\left(\frac{1}{2}+\frac{(4/3)B_{SO}+B_\phi}{B}\right)\right]\end{aligned} \tag{2.20}$$

where ψ is the digamma function, B_ϕ, B_{SO} and B_e are the characteristic field B_i linked to characteristic lengths l_i (distances) of **phase coherence**, electron traveled before being disturbed by spin-orbit interaction and elastic mean free path, respectively, by $B_i = \hbar/4el_i^2$.

In the limit of strong SOC, Eq. 2.20 reduces to

$$\Delta G(B) = \alpha\frac{e^2}{2\pi^2\hbar}\left[\ln\left(\frac{B_\phi}{B}\right) - \psi\left(\frac{1}{2}+\frac{B_\phi}{B}\right)\right] \tag{2.21}$$

where α is a coefficient indicating the type of localization, namely $\alpha < 0$ for weak localization and $\alpha > 0$ for weak anti-localization [64]. For the thinnest film ($t = 2.7$ nm, device B) in which the surface contributes the most, we analyzed the effect of FM states on the longitudinal magnetoconductance (MC). The temperature variation of $\Delta G(B) = G(B) - G(0\text{T})$, exhibits a crossover between WAL and WL at low B field region due to the competition between thermal fluctuations $k_B T$ and spontaneous magnetizations that randomize and align the orientation of magnetic moments, respectively (Fig. 2.17a).

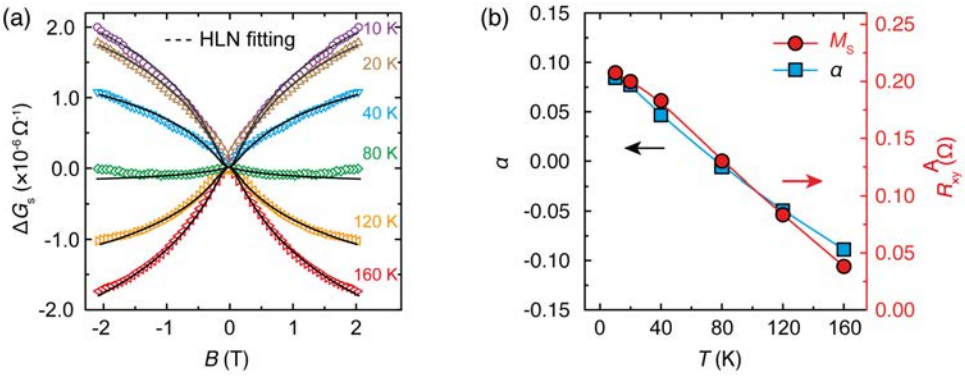

Figure 2.17 (a) Fitting the temperature dependence of the magnetoconductance of device B by the Hikami-Larkin-Nagaoka (HLN) equation. **(b)** Correlation between the α prefactor (black) used in the HLN equation and saturation magnetization M_s (red) derived from the AHE.

Table 2.1 Fitting parameters with HLN equation of the low field magnetoconductance data at various temperatures

T (K)	5	10	20	40	80	120	160
α	0.085	0.085	0.078	0.047	-0.006	-0.050	-0.089
B_ϕ (T)	0.051	0.051	0.052	0.053	0.028	0.055	0.064
l_ϕ (nm)	56.85	56.85	56.30	55.77	76.32	54.87	50.89

We next turn to a more quantitative analysis of the observed MC crossover phenomena. Considering our gating effect is a surface effect, hence the induced ferromagnetism as well as other transport phenomena should be confined within two dimensions. Applying HLN equation to analyze this crossover behavior, we derived that the temperature dependence of the fitting coefficient α scales linearly with the anomalous Hall resistance R_{xy}^{A}, demonstrating a close correlation between the electrical transport and the magnetization M at the surface of Pt films (Fig. 2.17b). This crossover resembles the behavior observed in magnetically doped topological insulators, where the surface states are also affected by the magnetization [65]. Consistently, the phase coherence length (l_ϕ ~50 nm) extracted from the HLN fitting (Tab. 2.1) is comparable with other surface magnetization systems [62, 65, 66].

Having a closer look at MC data in the full B field range (Fig. 2.18a), we notice that the profile of the B dependence is highly nonlinear. At low field range ($|B| < 2$ T), it shows crossover of MC, from positive MC at low temperature to negative MC at high temperature. At high field range ($|B| > 4$ T), the MC shows linear dependence on B field. At low temperature, the MC at high field shows positive slope. With the increase of temperature, this high field slope gradually decreases and becomes almost flat. For both variations in high and low field features, there is a transitional region between 2 T $< |B| <$ 4 T.

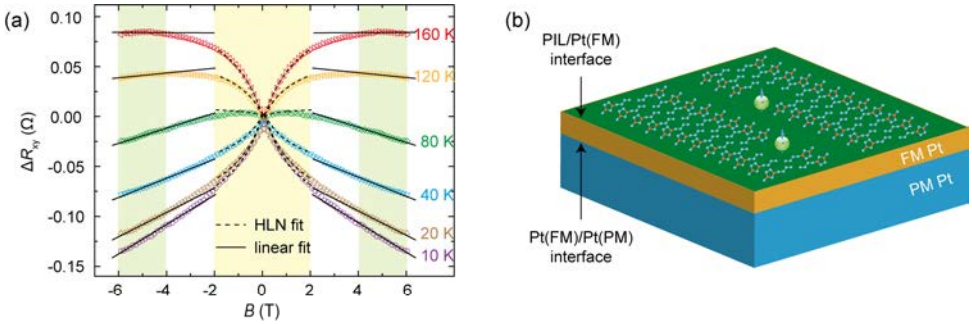

Figure 2.18 (a) The longitudinal transport data of Pt thin film of t = 2.7 nm. **(b)** Schematic illustration of the PIL-gated Pt device. It contains two interfaces, which are the PIL/topmost ferromagnetic (FM) Pt interface and the topmost FM Pt/bulk paramagnetic (PM) Pt interface.

The reason of complex transport data in our system is mainly due to mixture of localization with other transport phenomena. The system contains electronically dissimilar topmost layer gated by PIL and bottom unperturbed film that maintains the intrinsic bulk properties of Pt. Moreover, it is worth noting that the transport might also be affected by the interfacial behavior between these two layers (Fig. 2.18b). Due to the strong screening effect in intrinsic metal, the bulk Pt beneath the topmost layer behaves as pristine Pt, showing the same positive MR (negative MC) as shown in Figure 2.17a. A very important point here is the temperature range. The MR of pristine Pt only persists up to 40 K, from which the MR becomes featureless. Therefore, large MR response even at 160 K is due to the surface state.

The top-most Pt becomes FM after being gated with PIL, showing a positive linear MC at large field. With increasing of temperature, the ferromagnetism gets weaker and this positive MC diminishes as well. The same behavior happens for thicker film as well, despite that at low temperature the negative MR is less observable, due to larger mixing of the positive MR from the bulk Pt (intrinsic WAL). However, at higher temperature, the positive MR is purely due to the surface Pt because the bulk shows nearly zero MR (Fig. 2.16a).

2.4.8 Scaling relationship of anomalous Hall effect in PIL-gated Pt and various other systems.

Quantitatively, the origin of the AHE can be analyzed by the **scaling relationship** between anomalous transverse resistivity (conductivity) ρ_{AH} (σ_{AH}) and longitudinal resistivity (conductivity) ρ_{xx} (σ_{xx}) in a power law form $\rho_{AH} \propto \rho_{xx}^{\gamma}$ [67]. The components of the conductivity tensor were derived by inversion of the resistivity tensor. For cubic symmetry, which is valid for the face-centered cubic structure of Pt and $B \parallel c$, we get

$$\sigma_{AH} = \frac{\rho_{AH}}{\rho_{xx}^2 + \rho_{xy}^2}, \tag{2.22}$$

and

$$\sigma_{xx} = \frac{\rho_{xx}}{\rho_{xx}^2 + \rho_{xy}^2}, \tag{2.23}$$

Here, ρ_{AH} is determined by extrapolating ρ_{xy} in the linear regime to zero field.

Figure 2.19 shows the scaling diagram of anomalous Hall effect in PIL-gated Pt compared to various other systems. Different kinds of markers denote the σ_{xx} and σ_{AH} for distinct systems while each marker of the same kind represents the value at various temperature. When $\gamma = 1$, *i.e.* $\rho_{AH} \propto \rho_{xx}$ ($\sigma_{AH} \propto \sigma_{xx}$), the **skew scattering** mechanism dominates [38]; whereas the case of $\gamma = 2$, *i.e.* $\rho_{AH} \propto \rho_{xx}^{2}$ ($\sigma_{AH} \propto$ const.), corresponds to the **side jump** mechanism [39]. The γ components in both of these extrinsic origins are temperature dependent.

Our PIL-gated Pt, however, displays a scaling relation $\sigma_{AH} \propto \sigma_{xx}^{\Upsilon}$ ($\gamma \gg 1$) that is different from any other system (Fig. 2.19). One reason is because Pt is a

metal so that the electrical conductivity σ_{xx} does not change too much with temperature. On the other hand, the amplitude of the anomalous Hall effect that corresponds to the strength of the ferromagnetism changes rapidly with varying the temperature, which causes a significant variation of σ_{AH}. With increasing temperature, σ_{AH} decreases significantly, which is distinct from the situation in conventional band ferromagnets [68].

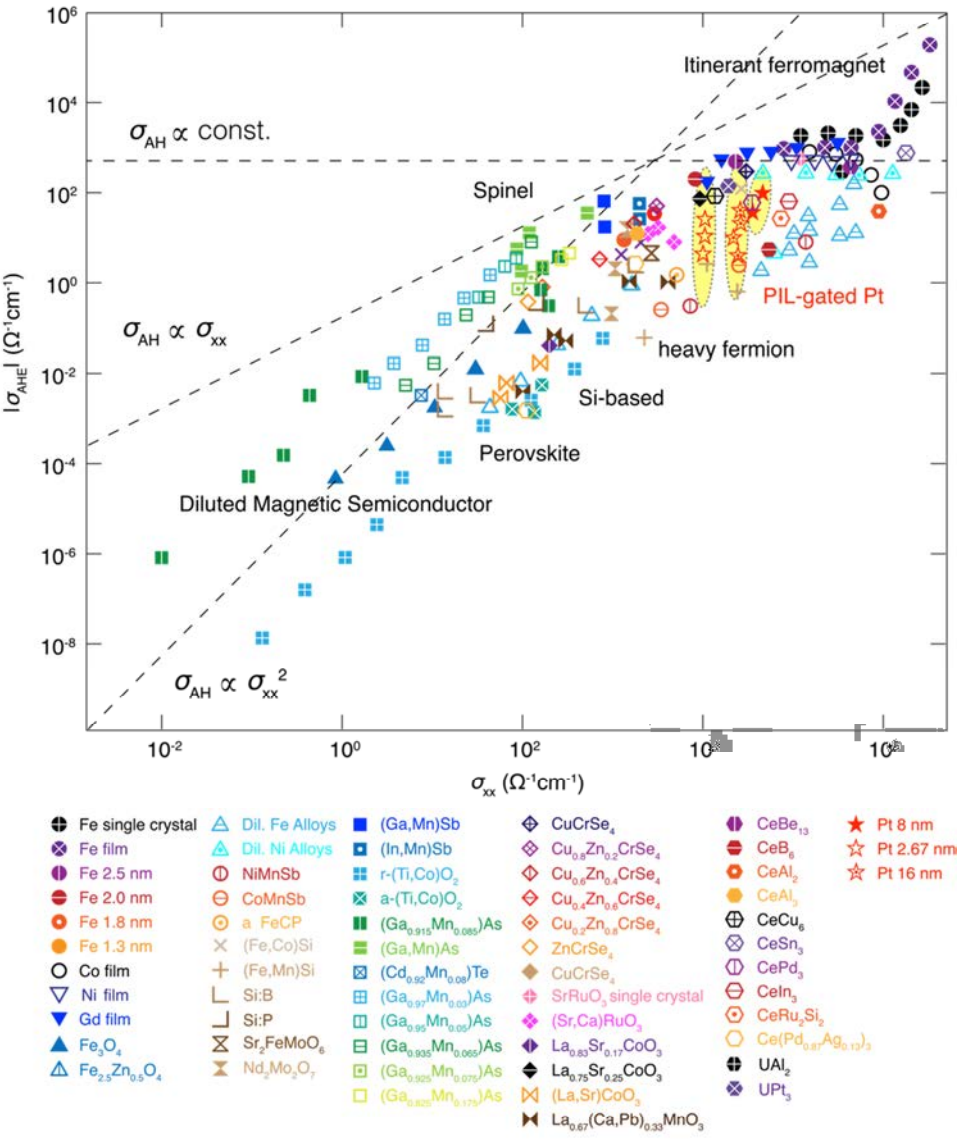

Figure 2.19 Scaling diagram of AHE for various magnetic systems. The AHE measured in PIL-gated Pt samples (shaded by yellow) are plotted together with many magentic systems reported previously **[73-76]**. The σ_{AH} measured for the FM state of Pt shows weak dependence on the σ_{xx}.

In addition, the behavior of σ_{AH} with respect to temperature strongly relies on the gating level V_G, which affects not only the change of σ_{xx}, but also σ_{AH}. The fact that σ_{AH} appears to be independent of σ_{xx} indicates that the induced ferromagnetism in Pt is intrinsic [69, 70]. When Pt is in the vicinity of a FM insulator, **yttrium iron garnet** (YIG), the AHE induced by the **magnetic proximity effect** (MPE) shows the opposite B field dependence, because the induced magnetic moments are anti-parallel to the magnetization of YIG [71, 72]. In contrast, the magnetization direction of the present system follows the B field. Both systems show the reversal of the ordinary Hall coefficient for ultrathin Pt films ($t < 3.0$ nm), which is consistent with the significant change of the band structure at reduced-dimensionality. In contrast to YIG, the strong Coulomb repulsion between anions in PIL sets large interionic distance, which prohibits FM **exchange interaction**. Hence, BMIM[$FeCl_4$] remains PM down to 2 K (Fig. 2.6b), which firmly excludes the MPE as the origin of the reported phenomena.

2.4.9 Magnetic phase diagram of PIL gated Pt

We determine the **saturation magnetization** of the PIL-gated Pt by extrapolating the linear part of R_{xy} under high B fields, where the anomalous Hall resistance R_{xy}^{A} that represents the M_s can be extracted (Fig. 2.20). The temperature dependence of M_s can be described by the ***Bloch*** **equation**

$$M_s = M_s(0)\left(1 - CT^{\beta}\right), \tag{2.24}$$

where $M_s(0)$ is the spontaneous magnetization at $T = 0$ K and β is the Bloch constant [77]. Fitting M_s for the film with $t = 2.7$ nm and thicker films ($t = 8.0$, 12.0, 16.0 nm) yielding $\beta = 1.3$ and 1.8, respectively. The similar β and resembling behavior of R_{xy}^{A} indicate that all FM samples of different thicknesses are likely originated from the same type of magnetization.

In general, T_c decreases with the increase of t. For sample A ($t = 8.0$ nm) optimized for the largest H_c, the extrapolated T_c is even above room temperature (300 K). In fact, the T_m of BMIM[$FeCl_4$] limits the upper-bound temperature of the induced FM state. Alternatively, choosing PILs with higher T_m might enable room temperature FM switching.

Interestingly, at low temperature (< 40 K), the M_s deviates from the Bloch equation, exhibiting an up-turn in accordance with the $1/T$ dependence. This behavior signals an effective field between the FM Pt layer and the paramagnetic $FeCl_4^-$ anions within the mean field theory, whose PM magnetization significantly increases at low temperature obeying **Curie's law**. It is worth noting that applying the same gating protocol to the identical Pt films using a conventional IL shows no ferromagnetism despite of the increased electrical conductivity (Fig. 2.16, Fig. S2.5) [58]. This clear difference indicates the importance of PIL in inducing the FM state in Pt.

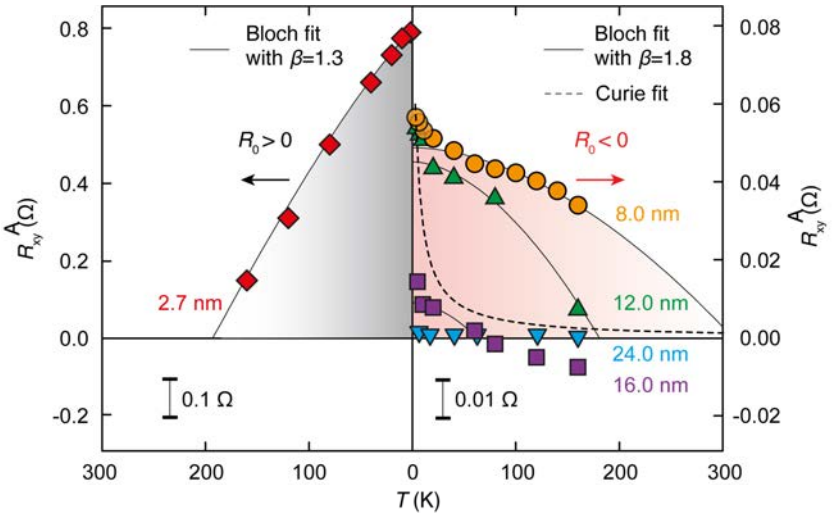

Figure 2.20 Magnetic phase diagram of M_s versus T jointed for gated Pt films of different thicknesses. The left panel indicates the ultrathin Pt film (t = 2.7 nm) with a positive ordinary Hall coefficient R_0. The right panel shows data from four individual thicknesses (8-24 nm), which all have a negative R_0. Gating effect becomes vague for films thicker than 16 nm. M_s of most temperature range follows the Bloch Law. At $T < 40$ K, M_s with $R_0 < 0$ displays an anomaly that can be fitted by Curie's law.

2.5 Supplementary information

2.5.1 Transport properties under negative ionic gate bias

We also measured the transport properties induced by negative V_G (Fig. S2.1). Negative gating accumulated magnetic anions on the surface of Pt film. Due to the strong screening of a typical metal, the accumulated anions deplete electrons at the top-most layer of Pt film. If AHE was mainly induced by **exchange interaction** between the carrier and the local moment of magnetic anion, the negative gating should induce even more pronounced FM state.

Conversely, negative gating only changes the slope $|R_{xy}/B|$ of linear Hall effect without inducing AHE (Fig. S2.1a). Moreover, the positive MR measured for negative V_G (Fig. S2.1b) is similar to that observed for pristine Pt (Fig. S2.1a), which is consistent with the absence of FM states.

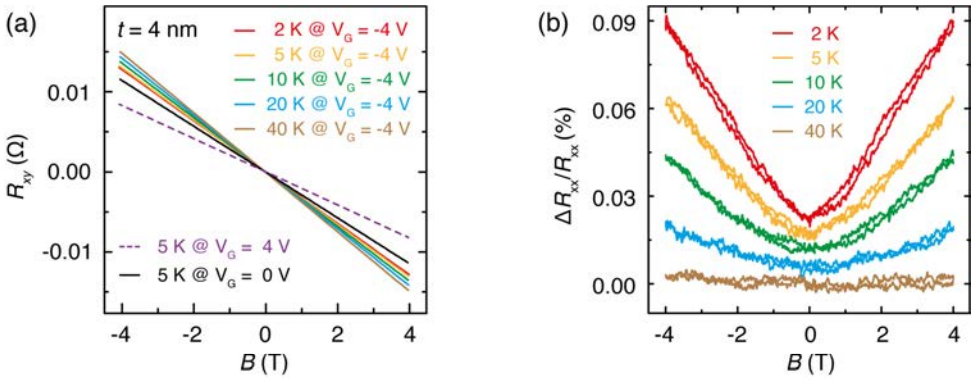

Figure S2.1 (a) Negative V_G decreases E_F, which increases the number of empty states in the 5*d*-band. In the transfer curve, the conductivity decreases due to more *s*-*d* scattering. Because of the opposite sign of n_h, the Hall conductivity R_{xy} changes consistently with different V_G. The Hall coefficients at 5 K change oppositely for positive V_G (brown) and negative V_G (orange) with respect to the pristine state (black). **(b)** In contrast to the negative MR in the positively gated state, the MR of the negatively gated sample behaves similar to its pristine state: positive MR at low temperature, which diminishes rapidly with increasing temperature. No ferromagnetism can be induced with negative V_G.

2.5.2 Transport properties of PIL-gated gold thin film

Gold (Au) is the element next to Pt with one more $5d$-electron, which fully fills the $5d$-band. Identical PIL gating was applied on Au film with $t = 8.0$ nm (Fig. S2.2a). The temperature dependence of R_s in five consecutive procedures was shown in Figure S2.2c: (1) Apply V_G at 220 K. (2) Cool device down to 2 K at 2 K min^{-1} and measure R_{xy} (state I). (3) Warm device up to 260 K at $V_G = 0$; the R_s coincided with the cooling down curve at $V_G = 3$ V until the ions become mobile again. At 220 K, the R_s (in red) has exactly the same value as that before gating (in black), indicating that the whole gating process is non-faradaic. (5) After fully relaxing the PIL at 260 K, the device was cooled down to 2 K without V_G. The R_{xy} was again measured at 2 K (state II).

Compared with Pt film of similar thickness, significant decrease of R_s at $V_G > 0$ was also observed. In spite of the similar V_G dependence of R_s, neither AHE (Fig. S2.2d) nor **Kondo effect** (chapter 3) (Fig. S2.2b) was observed in PIL-gated Au down to 2 K. The absence of FM state in Au after PIL gating is consistent with its fully filled $5d$-band and the band-filling scheme mentioned in Fig. 2.10.

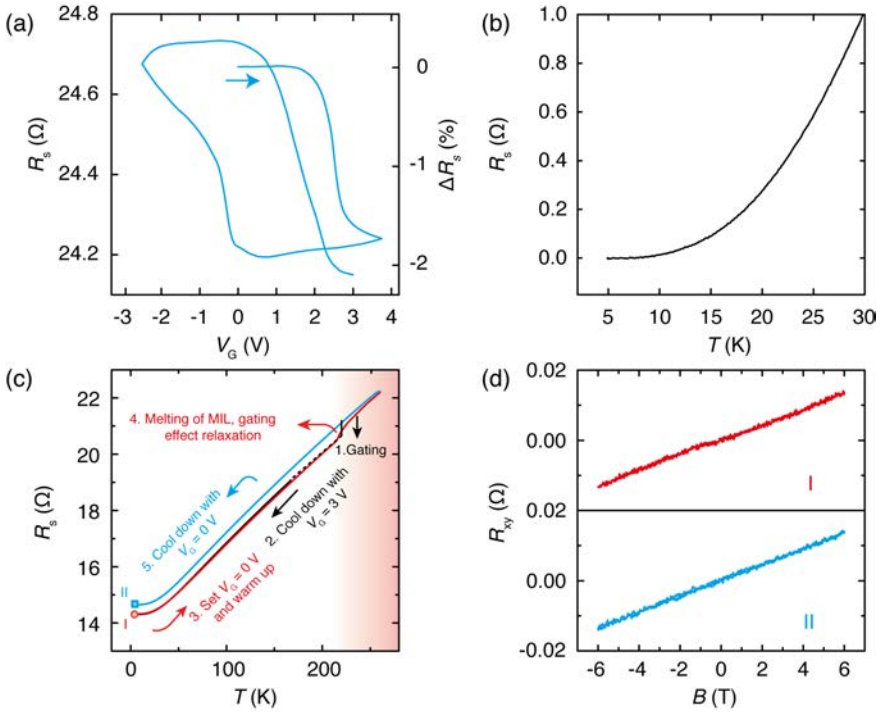

Figure S2.2 (a) Transfer curve of Au gated with a V_G sweep rate of 50 mV s^{-1} between 4 and -3 V. **(b)** Normalized sheet resistance R_s in the low temperature range shows no Kondo signature. **(c)** Temperature dependence of R_s in five consecutive procedures. **(d)** The Hall effects measured at state I and state II reveals that Au film does not show any clear AHE feature regardless of applying the V_G.

2.5.3 Transport properties of PIL-gated palladium film

Beside Pt and Au, the identical PIL gating was also applied to **palladium** (Pd), another typical exchange-enhanced metal. As shown in Fig. S2.3, the PIL gating of a Pd film (t = 5.0 nm) can also induce FM state. Comparing with the Pt film of similar thickness, we briefly summarize the major consistent behaviors as follows:

1) At low temperature (5 K), the pristine or unbiased (V_G = 0) Pd film shows positive MR (Fig. S2.3a) and ordinary Hall effect (Fig. S2.3c).
2) PIL gating switches the MR from positive to overall negative MR after the emergence of AHE (Fig. 2.3b).
3) The PIL gating induces FM state with clear **coercive loop** in AHE (Fig. 2.3d).

In spite of the similarities, quantitatively, the MR of PIL-gated Pd shows much more pronounced hysteresis in the low field regime (Fig. 2.3c), where the AHE effect also shows hysteresis loop (Fig. S2.3d).

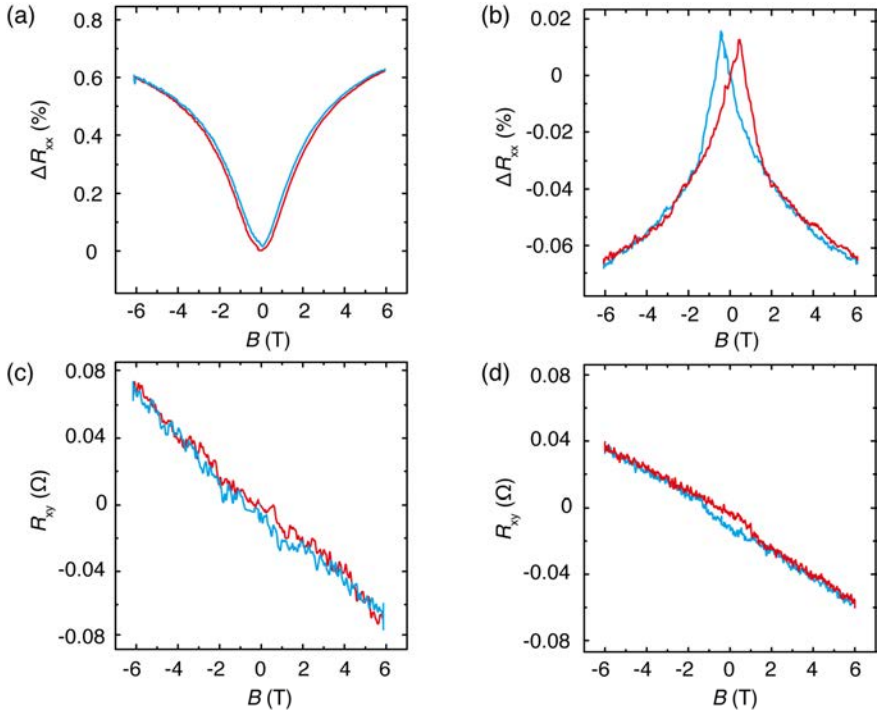

Figure S2.3 Low temperature (T = 5 K) electrical transport of pristine and PIL-gated Pd thin films. **(a)** Pristine Pd film shows a weak anti-localization in MR. **(b)** Pristine Pd shows ordinary Hall effect. **(c)** Longitudinal MR shows butterfly-shaped hysteresis due to FM state. **(d)** The Hall effect measurement shows AHE with a hysteresis loop within ±2 T, in consistent with the size of hysteresis found longitudinal MR.

The clear butterfly shape in MR indicates the randomization of magnetic domains close to the switching of the magnetization direction. On the other hand, the **hysteresis loop** in AHE (Fig. S2.3d) is smaller compared to Pt. The strength of spin-orbit interaction (Eq. 2.17) in Pd is ~4.78 time smaller than Pt, which might play a role in the different AHE behavior [78, 79].

Nevertheless, inducing FM state also in Pd indicates the universality of the PIL gating technique as an effective methodology for inducing FM states. The full results will be detailed in an independent paper. Despite the quantitative differences, the highly consistent FM state suggests that our proposed physical picture might be universal to Stoner enhanced elements.

2.5.4 Transport properties of Pt thin film doped with Fe impurity

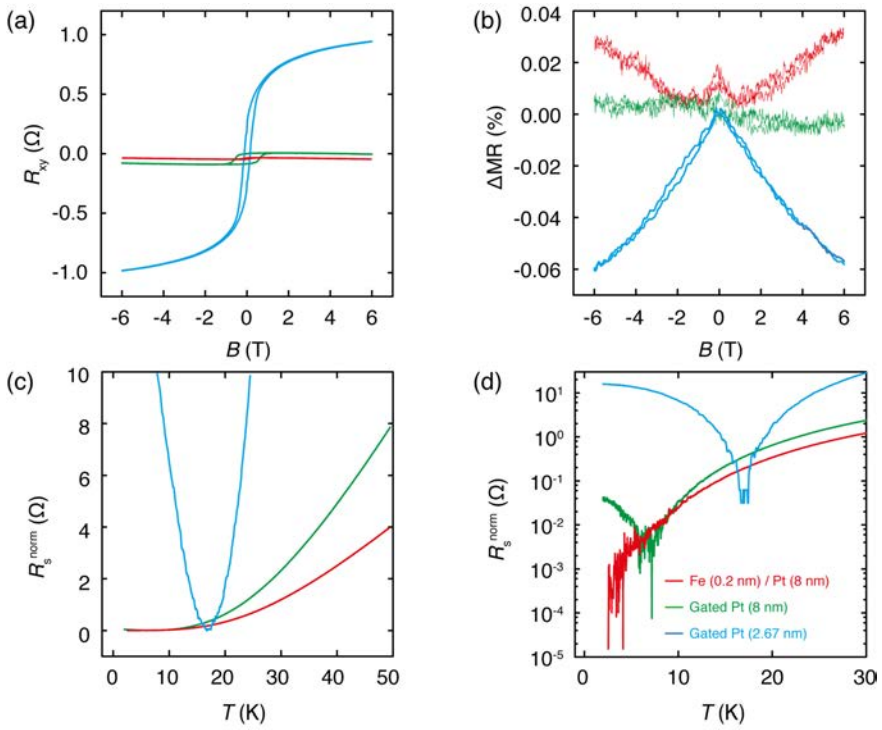

Figure S2.4 Comparison between Fe impurity-doped and PIL-gated Pt thin films. **(a)** Temperature dependence of sheet resistance at low temperature on a linear scale. **(b)** Temperature dependence of sheet resistance at low temperature on a logarithmic scale. The Pt sample with Fe impurities does not show a Kondo effect, which is in sharp contrast with both gated counterparts. **(c)** The anomalous Hall signal observed in the sample with Fe impurities is negligibly small compared with the PIL-gated systems. **(d)** The MR of the sample with Fe impurities is also distinct from those measured for PIL-gated Pt films, in which the former shows a positive MR with weak localization behavior in small fields, while the latter shows negative MR.

To firmly remove the possibility of having trace of Fe impurities after PIL gating, we prepared a Pt film with Fe impurities (0.2 nm nominal thickness) intentionally evaporated *in-situ* prior to the deposition of Pt film. Compare to the PIL-gated Pt film of identical thickness (8.0 nm), the Pt film with Fe contamination shows negligibly weak ferromagnetism (Fig. S2.4a).

The Fe/Pt film shows negative MR at small B field ($|B| < 1$ T), indicating typical **weak localization** behavior. This is consistent with the presence of Fe impurities (red curve in Fig. S2.4b). Under larger field ($|B| > 1$ T), the positive MR is consistent with the conventional dependence of $R_s \propto \mu B^2$. In contrast, the MR of PIL-gated Pt film shows distinct behaviors. There is a clear crossover from positive to negative MR with the decrease of film thickness. The very thin film ($t = 2.7$ nm) shows negative MR (blue curve in Fig. S2.4b), while the thicker Pt films ($t > 8$ nm) show positive MR. Since the PIL gating only affects the surface of the Pt films, the MR of the bulk remains positive regardless of the film thickness. Therefore, thinner film has less contribution from the bulk positive MR. The featureless MR observed for film of $t = 8.0$ nm might come from the compensation between these two opposite MR dependences (green curve in Fig. S2.4b).

In addition to the contrasting magnetization and MR dependence, the Fe doped Pt film shows no **Kondo effect** at low temperature (Fig. S2.4c,d). We will discuss more about the Kondo effect in chapter 3.

In summary, contaminating the Pt film by introducing Fe impurities cannot reproduce the effect of PIL gating, which suggest that the gate induced FM state cannot be ascribed to Fe contamination.

2.5.5 Gating cycles with sequential switch between PIL and conventional IL

As a control experiment for clarifying what are the essential ingredients for inducing FM state, we performed gating cycles by switching the gating media between conventional IL that contains non-magnetic ions (DEME-TFSI) and PIL (BMIM[$FeCl_4$]) on the same Pt film ($t = 12.0$ nm). As shown in Fig. S2.5, a series of measurements shown in panel A to E is grouped in different step 1 and 2 for gating with IL and PIL, respectively. Therefore, each measurement on the sequential change of sample status can be easily tracked by labeling cycle/step/panel in the matrix (Fig. S2.5).

For gating with both IL (C1/S1/B) and PIL (C1/S2/B), although the V_G dependence of the R_s show similar substantial decrease with the increase of V_G, the AHE from FM state was induced only by the PIL gating (red line, C1/S2/D) in contrast to the ordinary Hall effect (C1/S1/D) observed by IL gating. To confirm that this FM state exists only after gating, we warmed the sample gated by PIL (C1/S2/D) up to the melting temperature of the PIL with $V_G = 0$ V (following the red line of C1/S2/C) to release the gating effect. Then the device was cooled down to 5 K again with $V_G = 0$ V (following the blue line of C1/S2/C). The Hall effect

measured thereafter shows linear field dependence without AHE (blue line, C1/S2/D). To remove the concern about the possible FM impurities produced by the PIL gating, we repeated IL gating on the same device immediately after washing away the PIL by acetone (C1/S2/E). The Hall signal (C2/S1/D) resumed the linear field dependence without AHE feature in consistent with the status access by the identical gating conditions using IL (C1/S1/D). By switching back to PIL, the FM state can be repeatedly induced as shown by the clear AHE signal (red curve, C2/S2/D). Again, melting the PIL can restore the linear Hall response (blue curve, C2/S2/D).

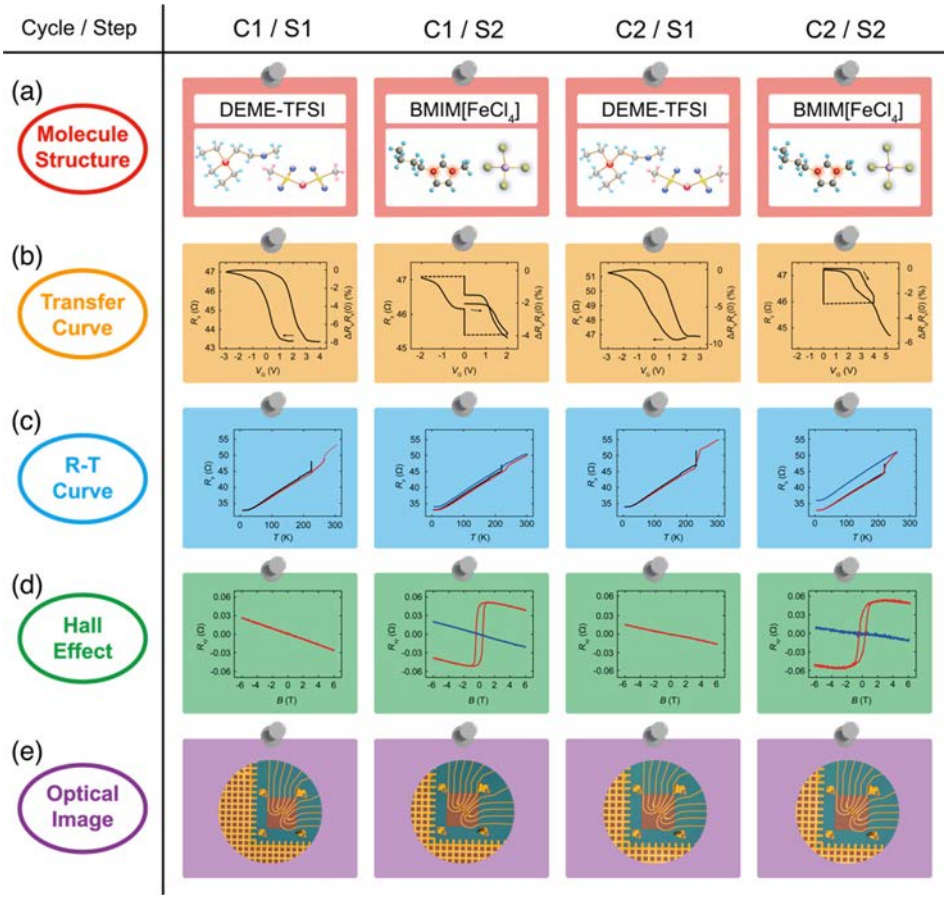

Figure S2.5 Diary of gating cycles by switching the gating media between non-magnetic IL and PIL on the same Pt film (t = 12.0 nm). **(a)** Schematic molecular structures of used ILs. **(b)** The V_G dependence of R_s for each gating procedure. **(c)** Temperature dependence of the R_s measured after each gating. **(d)** The Hall effect measured at 5 K after each cooling down, where the different color matches the color of temperature dependence of R_s of the cooling procedure (red for $V_G > 0$, blue for $V_G = 0$). **(e)** Optical images taken after each measurement. The ionic liquid was washed away by acetone and the device was cleaned by isopropanol.

In conclusion, the reversible behavior observed in consecutive gating cycles using different liquids not only clearly shows the indispensable role of PIL gating but also excludes Fe contamination as the possible origin of the induced FM state.

2.5.6 Optical and atomic force microscopy of Pt film before and after gating

The sample status at each step of the gating cycles is closely monitored by optical and **atomic force microscopy** (AFM) as shown in Figure S2.5e and Figure S2.6a, b. The AFM images are all measured in tapping mode (Bruker Nano MultiMode 8-HR) for characterizing the surface morphology and sample thickness.

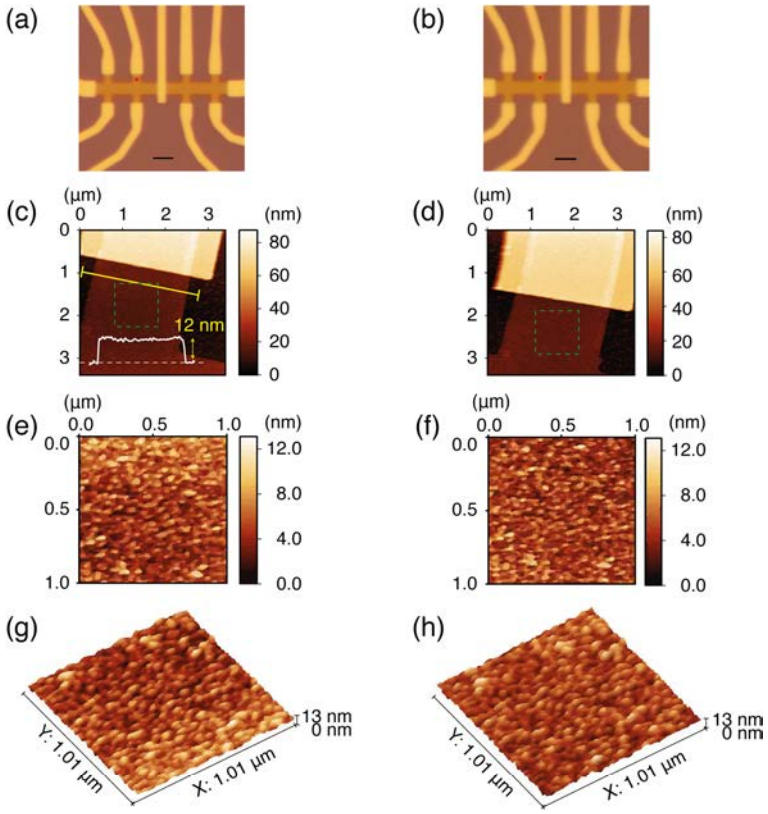

Figure S2.6 Surface morphology of Pt film before and after PIL gating. Optical images of the Pt sample before applying the PIL **(a)** and after gating with the PIL **(b)**. In both panels **(a)** and **(b)**, the scale bars correspond to a length of 5 μm. AFM imaging of the Pt film surface were performed within the areas marked by red dots. Along the yellow line in panel **(c)**, the height profile (white) of the film shows that the thickness of the film is 12.0 nm. The surface morphology is shown for the areas within green rectangles in panel **(c)** and **(d)** for the sample before **(e)** and after **(f)** PIL gating. Corresponding bird's eye views of the surface morphology are also shown before **(g)** and after **(h)** PIL gating. It is worth noting that most of the fine details of the sample remains identical before and after gating.

For the Pt sample of t = 12.0 nm (Fig. S2.6c), the root mean square (R_{ms}) of the surface roughness from 1×1 μm^2 scanned area was 1.7 nm (Fig. S2.6e, f). The surface roughness is closely related to the deposition technique and the flux rate. In general, magnetron sputtering produces films with better crystallinity but rougher surface compared to the film prepared by e-beam evaporation [80]. For all Pt films measured before and after gating, no clear difference could be resolved for the morphology of Pt surface (Fig. S2.6e, f, g, h).

2.6 Summary

In this chapter, we study the paramagnetic ionic gating induced ferromagnetism in Pt thin film comprehensively, revealed as anomalous Hall effect (AHE). By introducing the paramagnetic ionic liquids as gating media, we demonstrated that ferromagnetic state can be reversibly switched ON and OFF in Stoner enhanced element, such as Pt and Pd.

The induced ferromagnetic state has been proven to be two-dimensional (2D), evidenced by the crossover behavior of the electron localization in the magnetoconductance measurement for the thinnest film.

With increase of the film thickness, the enlarged bulk conduction acts as short circuit bypassing the surface channel, which diminishes the ferromagnetic signal, such as anomalous Hall effect and negative magnetoresistance.

A series of control experiments have firmly confirmed the electrostatic nature of the gating, in which magnetic impurities should not be the reason causing the emergent surface spontaneous magnetization.

The magnitude of induced FM state depends on the gate voltage as well as temperature. From the fitting of the temperature dependence of saturation magnetization, the Curie temperature can exceed the room temperature.

Although an explicit fundamental theory remains an open issue, phenomenologically, the emergence of the 2D ferromagnetism in Stoner exchange metal thin film requires the combination of large charge accumulation in presence of paramagnetic moments. Scaling analysis of the AHE proves the intrinsic origin of the FM state.

2.7 References

[1] Ohno H, Chiba D, Matsukura F, Omiya T, Abe E, Dietl T, "Electric-field control of ferromagnetism", *Nature* **408**, 944 (2000).

[2] Weisheit M, Fahler S, Marty A, Souche Y, Poinsignon C, Givord D, "Electric field-Induced modification of magnetism in thin-film ferromagnets", *Science* **315**, 349-51 (2007).

[3] Chiba D, Fukami S, Shimamura K, Ishiwata N, Kobayashi K, Ono T, "Electrical control of the ferromagnetic phase transition in cobalt at room temperature", *Nat Mater* **10**, 853-6 (2011).

[4] Matsukura F, Tokura Y, Ohno H, "Control of magnetism by electric fields", *Nat Nanotechnol* **10**, 209-20 (2015).

[5] Chiba D, Yamanouchi M, Matsukura F, Ohno H, "Electrical manipulation of magnetization reversal in a ferromagnetic semiconductor", *Science* **301**, 943 (2003).

[6] Dietl T, "A ten-year perspective on dilute magnetic semiconductors and oxides", *Nat Mater* **9**, 965-74 (2010).

[7] Yamada Y, Ueno K, Fukumura T, Yuan HT, Shimotani H, Iwasa Y, Gu L, Tsukimoto S, Ikuhara Y, Kawasaki M, "Electrically induced ferromagnetism at room temperature in cobalt-doped titanium dioxide", *Science* **332**, 1065-7 (2011).

[8] Kimura T, Goto T, Shintani H, Ishizaka K, Arima T, Tokura Y, "Magnetic control of ferroelectric polarization", *Nature* **426**, 55-8 (2003).

[9] Eerenstein W, Mathur ND, Scott JF, "Multiferroic and magnetoelectric materials", *Nature* **442**, 759-65 (2006).

[10] Cheong S-W, Mostovoy M, "Multiferroics: a magnetic twist for ferroelectricity", *Nat Mater* **6**, 13-20 (2007).

[11] Ye JT, Inoue S, Kobayashi K, Kasahara Y, Yuan HT, Shimotani H, Iwasa Y, "Liquid-gated interface superconductivity on an atomically flat film", *Nat Mater* **9**, 125-8 (2009).

[12] Ye JT, Zhang YJ, Akashi R, Bahramy MS, Arita R, Iwasa Y, "Superconducting dome in a gate-tuned band insulator", *Science* **338**, 1193-6 (2012).

[13] Lu JM, Zheliuk O, Leermakers I, Zeitler U, Yuan N, Ye JT, "Evidence for two-dimensional Ising superconductivity in gated MoS_2", *Science* **350**, 1353 (2015).

[14] Zhang YJ, Oka T, Suzuki R, Ye JT, Iwasa Y, "Electrically switchable chiral light-emitting transistor", *Science* **344**, 725-8 (2014).

[15] Wang QH, Kalantar-Zadeh K, Kis A, Coleman JN, Strano MS, "Electronics and optoelectronics of two-dimensional transition metal dichalcogenides", *Nat Nanotechnol* **7**, 699-712 (2012).

[16] Maruyama T, Shiota Y, Nozaki T, Ohta K, Toda N, Mizuguchi M, Tulapurkar AA, Shinjo T, Shiraishi M, Mizukami S, Ando Y, Suzuki Y, ″Large voltage-induced magnetic anisotropy change in a few atomic layers of iron″, *Nat Nanotechnol* **4**, 158-61 (2009).

[17] Shimamura K, Chiba D, Ono S, Fukami S, Ishiwata N, Kawaguchi M, Kobayashi K, Ono T, ″Electrical control of Curie temperature in cobalt using an ionic liquid film″, *Appl Phys Lett* **100**, 122402 (2012).

[18] Petach TA, Lee M, Davis RC, Mehta A, Goldhaber-Gordon D, ″Mechanism for the large conductance modulation in electrolyte-gated thin gold films″, *Phys Rev B* **90**, 081108 (2014).

[19] Obinata A, Hibino Y, Hayakawa D, Koyama T, Miwa K, Ono S, Chiba D, ″Electric-field control of magnetic moment in Pd″, *Sci Rep* **5**, 14303 (2015).

[20] Xiong ZH, Wu D, Vardeny ZV, Shi J, ″Giant magnetoresistance in organic spin-valves″, *Nature* **427**, 821-4 (2004).

[21] Ma'Mari FA, Moorsom T, Teobaldi G, Deacon W, Prokscha T, Luetkens H, Lee S, Sterbinsky GE, Arena DA, MacLaren DA, Flokstra M, Ali M, Wheeler MC, Burnell G, Hickey BJ, Cespedes O, ″Beating the Stoner criterion using molecular interfaces″, *Nature* **524**, 69-73 (2015).

[22] Bernien M, Miguel J, Weis C, Ali ME, Kurde J, Krumme B, Panchmatia PM, Sanyal B, Piantek M, Srivastava P, Baberschke K, Oppeneer PM, Eriksson O, Kuch W, Wende H, ″Tailoring the nature of magnetic coupling of Fe-porphyrin molecules to ferromagnetic substrates″, *Phys Rev Lett* **102**, 047202 (2009).

[23] Zhang X, Mizukami S, Kubota T, Oogane M, Naganuma H, Ando Y, Miyazaki T, ″Interface effects on perpendicular magnetic anisotropy for molecular-capped cobalt ultrathin films″, *Appl Phys Lett* **99**, 162509-4 (2011).

[24] Raman KV, Kamerbeek AM, Mukherjee A, Atodiresei N, Sen TK, Lazić P, Caciuc V, Michel R, Stalke D, Mandal SK, Blügel S, Münzenberg M, Moodera JS, ″Interface-engineered templates for molecular spin memory devices″, *Nature* **493**, 509-13 (2013).

[25] Hall EH, ″On a new action of the magnet on electric currents″, *Am J Math* **2**, 287 (1879).

[26] Hall EH, ″XVIII. On the "Rotational Coefficient" in nickel and cobalt″, *Philos Mag* **12**, 157-72 (1881).

[27] Dyakonov MI, Perel VI, ″Current-induced spin orientation of electrons in semiconductors″, *Phys Lett A* **35**, 459-60 (1971).

[28] Kato YK, Myers RC, Gossard AC, Awschalom DD, ″Observation of the spin Hall effect in semiconductors″, *Science* **306**, 1910-3 (2004).

[29] von Klitzing K, Dorda G, Pepper M, ″New method for high-accuracy determination of the fine-structure constant based on quantized Hall resistance″, *Phys Rev Lett* **45**, 494 (1980).

[30] Willett R, Eisenstein JP, Stormer HL, Tsui DC, Gossard AC, English JH, ″Observation of an even-denominator quantum number in the fractional quantum Hall effect″, *Phys Rev Lett* **59**, 1776 (1987).

[31] Kalmeyer V, Laughlin RB, ″Equivalence of the resonating-valence-bond and fractional quantum Hall states″, *Phys Rev Lett* **59**, 2095 (1987).

[32] Bernevig BA, Zhang S-C, ″Quantum spin Hall effect″, *Phys Rev Lett* **96**, 106802 (2006).

[33] König M, Wiedmann S, Brüne C, Roth A, Buhmann H, Molenkamp LW, Qi X-L, Zhang S-C, ″Quantum spin Hall insulator state in HgTe quantum wells″, *Science* **318**, 766-70 (2007).

[34] Kane CL, Mele EJ, ″Quantum spin Hall effect in graphene″, *Phys Rev Lett* **95**, 226801-4 (2005).

[35] Chang CZ, Zhang J, Feng X, Shen J, Zhang Z, Guo M, Li K, Ou Y, Wei P, Wang LL, Ji ZQ, Feng Y, Ji S, Chen X, Jia J, Dai X, Fang Z, Zhang SC, He K, Wang Y, Lu L, Ma XC, Xue QK, ″Experimental observation of the quantum anomalous Hall effect in a magnetic topological insulator″, *Science* **340**, 167-70 (2013).

[36] Karplus R, Luttinger JM, ″Hall effect in ferromagnetics″, *Phys Rev* **95**, 1154-60 (1954).

[37] Chang M-C, Niu Q, ″Berry phase, hyperorbits, and the Hofstadter spectrum: semiclassical dynamics in magnetic Bloch bands″, *Phys Rev B* **53**, 7010 (1996).

[38] Smit J, ″The spontaneous Hall effect in ferromagnetics I″, *Physica* **21**, 877-87 (1955).

[39] Berger L, ″Side-jump mechanism for the Hall effect of ferromagnets″, *Phys Rev B* **2**, 4559-66 (1970).

[40] Del Sesto RE, McCleskey TM, Burrell AK, Baker GA, Thompson JD, Scott BL, Wilkes JS, Williams P, ″Structure and magnetic behavior of transition metal based ionic liquids″, *Chem Commun* **0**, 447-9 (2008).

[41] Su YZ, Fu YC, Yan JW, Chen ZB, Mao BW, ″Double layer of Au(100)/ionic liquid interface and its stability in imidazolium - based ionic liquids″, *Angew Chem* **121**, 5250-3 (2009).

[42] Sakuragi S, Sakai T, Urata S, Aihara S, Shinto A, Kageshima H, Sawada M, Namatame H, Taniguchi M, Sato T, ″Thickness-dependent appearance of ferromagnetism in Pd(100) ultrathin films″, *Phys Rev B* **90**, 054411-5 (2014).

[43] Sakamoto Y, Oba Y, Maki H, Suda M, Einaga Y, Sato T, Mizumaki M, Kawamura N, Suzuki M, ″Ferromagnetism of Pt nanoparticles induced by surface chemisorption″, *Phys Rev B* **83**, 104420-13 (2011).

[44] MacDonald AH, Daams JM, Vosko SH, Koelling DD, ″Influence of relativistic contributions to the effective potential on the electronic structure of Pd and Pt″, *Phys Rev B* **23**, 6377-98 (1981).

[45] Windmiller LR, ″Experimental determination of the Fermi radius, velocity, and g factor in Pd and Pt″, *J Appl Phys* **40**, 1291 (1969).

[46] Andersen OK, ″Electronic Structure of the fcc Transition Metals Ir, Rh, Pt, and Pd″, *Phys Rev B* **2**, 883-906 (1970).

[47] Fischer G, Hoffmann H, Vancea J, ″Mean free path and density of conductance electrons in platinum determined by the size effect in extremely thin films″, *Phys Rev B* **22**, 6065-73 (1980).

[48] Moruzzi VL, Janak JF, Williams AR, "*Calculated Electronic Properties of Metals*", Pergamon, New York (2013)

[49] Sagmeister M, Brossmann U, Landgraf S, Würschum R, ″Electrically tunable resistance of a metal″, *Phys Rev Lett* **96**, 156601 (2006).

[50] Carcia PF, ″Perpendicular magnetic anisotropy in Pd/Co and Pt/Co thin-film layered structures″, *J Appl Phys* **63**, 5066-9 (1988).

[51] Nakajima N, Koide T, Shidara T, Miyauchi H, ″Perpendicular magnetic anisotropy caused by interfacial hybridization via enhanced orbital moment in Co/Pt multilayers: magnetic circular x-ray dichroism study″, *Phys Rev* **81**, 5229 (1998).

[52] Tang C, Sellappan P, Liu Y, Xu Y, Garay JE, Shi J, ″Anomalous Hall hysteresis in $Tm_3Fe_5O_{12}$/Pt with strain-induced perpendicular magnetic anisotropy″, *Phys Rev B* **94**, 140403 (2016).

[53] Jeong J, Ferrante Y, Faleev SV, Samant MG, Felser C, Parkin SSP, ″Termination layer compensated tunnelling magnetoresistance in ferrimagnetic Heusler compounds with high perpendicular magnetic anisotropy″, *Nat Commun* **7**, 10276 (2016).

[54] Navas D, Redondo C, Badini Confalonieri GA, Batallan F, Devishvili A, Iglesias-Freire Ó, Asenjo A, Ross CA, Toperverg BP, ″Domain-wall structure in thin films with perpendicular anisotropy: Magnetic force microscopy and polarized neutron reflectometry study″, *Phys Rev B* **90**, 054425-12 (2014).

[55] Maat S, Takano K, Parkin S, Fullerton EE, ″Perpendicular exchange bias of Co/Pt multilayers″, *Phys Rev Lett* **87**, 087202 (2001).

[56] Ikeda S, Miura K, Yamamoto H, Mizunuma K, Gan HD, Endo M, Kanai S, Hayakawa J, Matsukura F, Ohno H, ″A perpendicular-anisotropy CoFeB--MgO magnetic tunnel junction″, *Nat Mater* **9**, 721-4 (2010).

[57] Franken JH, Swagten HJM, Koopmans B, ″Shift registers based on magnetic domain wall ratchets with perpendicular anisotropy″, *Nat Nanotechnol* **7**, 499 (2012).

[58] Shimizu S, Takahashi KS, Hatano T, Kawasaki M, Tokura Y, Iwasa Y, ″Electrically tunable anomalous Hall effect in Pt thin films″, *Phys Rev Lett* **111**, 216803 (2013).

[59] Nakayama H, Ye J, Ohtani T, Fujikawa Y, Ando K, Iwasa Y, Saitoh E, ″Electroresistance effect in gold thin film induced by ionic-liquid-gated electric double layer″, *Appl Phys Express* **5**, 023002 (2012).

[60] Hong SC, Lee JI, Wu R, ″Ferromagnetism in Pd thin films induced by quantum well states″, *Phys Rev B* **75**, 172402-4 (2007).

[61] Nagaosa N, Sinova J, Onoda S, MacDonald AH, Ong NP, ″Anomalous Hall effect″, *Rev Mod Phys* **82**, 1539-92 (2010).

[62] Shiomi Y, Ohtani T, Iguchi S, Sasaki T, Qiu Z, Nakayama H, Uchida K, Saitoh E, ″Interface-dependent magnetotransport properties for thin Pt films on ferrimagnetic $Y_3Fe_5O_{12}$″, *Appl Phys Lett* **104**, 242406-6 (2014).

[63] Gong S-J, Cai J, Yao Q-F, Tong W-Y, Wan X, Duan C-G, Chu JH, ″Orbital control of Rashba spin orbit coupling in noble metal surfaces″, *J Appl Phys* **119**, 125310 (2016).

[64] Hikami S, Larkin AI, Nagaoka Y, ″Spin-orbit interaction and magnetoresistance in the two dimensional random system″, *Prog Theor Phys* **63**, 707-10 (1980).

[65] Liu M, Zhang J, Chang C-Z, Zhang Z, Feng X, Li K, He K, Wang L-L, Chen X, Dai X, Fang Z, Xue Q-K, Ma X, Wang Y, ″Crossover between weak antilocalization and weak localization in a magnetically doped topological insulator″, *Phys Rev Lett* **108**, 036805 (2012).

[66] Gang T, Yilmaz MD, Ataç D, Bose SK, Strambini E, Velders AH, de Jong MP, Huskens J, van der Wiel WG, ″Tunable doping of a metal with molecular spins″, *Nat Nanotechnol* **7**, 232-6 (2012).

[67] Tian Y, Ye L, Jin X, ″Proper Scaling of the Anomalous Hall Effect″, *Phys Rev Lett* **103**, 087206 (2009).

[68] Miyasato T, Abe N, Fujii T, Asamitsu A, Onoda S, Onose Y, Nagaosa N, Tokura Y, ″Crossover behavior of the anomalous Hall effect and anomalous Nernst effect in itinerant ferromagnets″, *Phys Rev Lett* **99**, 086602 (2007).

[69] Luttinger JM, ″Theory of the Hall effect in ferromagnetic substances″, *Phys Rev* **112**, 739-51 (1958).

[70] Nagaosa N, ″Anomalous Hall effect–a new perspective–″, *J Phys Soc Jpn* **75**, 042001 (2006).

[71] Meyer S, Schlitz R, Geprägs S, Opel M, Huebl H, Gross R, Goennenwein STB, ″Anomalous Hall effect in YIG|Pt bilayers″, *Appl Phys Lett* **106**, 132402-5 (2015).

[72] Lu YM, Choi Y, Ortega CM, Cheng XM, Cai JW, Huang SY, Sun L, Chien CL, ″Pt magnetic polarization on $Y_3Fe_5O_{12}$ and magnetotransport characteristics″, *Phys Rev Lett* **110**, 147207 (2013).

[73] Toyosaki H, Fukumura T, Yamada Y, Nakajima K, Chikyow T, Hasegawa T, Koinuma H, Kawasaki M, ″Anomalous Hall effect governed by electron doping in a room-temperature transparent ferromagnetic semiconductor″, *Nat Mater* **3**, 221-4 (2004).

[74] Manyala N, Sidis Y, DiTusa JF, Aeppli G, Young DP, Fisk Z, ″Large anomalous Hall effect in a silicon-based magnetic semiconductor″, *Nat Mater* **3**, 255-62 (2004).

[75] Fukumura T, Toyosaki H, Ueno K, Nakano M, Yamasaki T, Kawasaki M, ″A scaling relation of anomalous Hall effect in ferromagnetic semiconductors and metals″, *Jpn J Appl Phys* **46**, L642 (2007).

[76] Chiba D, Werpachowska A, Endo M, Nishitani Y, Matsukura F, Dietl T, Ohno H, ″Anomalous Hall effect in field-effect structures of (Ga,Mn)As″, *Phys Rev Lett* **104**, 106601 (2010).

[77] Blundell S, "*Magnetism in condensed matter*", Oxford University Press Inc., New York (2001)

[78] Guo GY, Murakami S, Chen TW, Nagaosa N, ″Intrinsic spin Hall effect in platinum: first-principles calculations″, *Phys Rev Lett* **100**, 096401 (2008).

[79] Guo GY, Niu Q, Nagaosa N, ″Anomalous Nernst and Hall effects in magnetized platinum and palladium″, *Phys Rev B* **89**, 214406 (2014).

[80] Vlietstra N, Shan J, Castel V, van Wees BJ, Ben Youssef J, ″Spin-Hall magnetoresistance in platinum on yttrium iron garnet: Dependence on platinum thickness and in-plane/out-of-plane magnetization″, *Phys Rev B* **87**, 184421 (2013).